Available online at www.sciencedirect.com
ScienceDirect
Comput. Methods Appl. Mech. Engrg. 387 (2021) 114165
Computer methods in applied mechanics and engineering
www.elsevier.com/locate/cma

Coupled elasto-viscoplastic and damage model accounting for plastic anisotropy and damage evolution dependent on loading conditions

R. Fincato*, S. Tsutsumi*

Joining and Welding Research Institute, Osaka University, 11-1, Mihogaoka, Ibaraki, Osaka, 567-0047, Japan

Received 7 July 2021; received in revised form 23 August 2021; accepted 29 August 2021
Available online 27 September 2021

Abstract

This work presents an unconventional fully coupled elasto-viscoplastic and damage constitutive model that is suitable for investigating the failure mechanism of metallic materials. The constitutive equations are developed within a finite elastoplasticity framework under the assumption of hypoelastic-based plasticity. Anisotropic plastic potential and plastic-induced anisotropy are modelled by means of the Hill48 yield criterion and a Chaboche-type non-linear kinematic hardening law, respectively. A modified Voce-type law is assumed for the isotropic hardening behaviour. A novel law is proposed to account for an evolution of the damage depending on the loading directions. The proposed model was implemented via user subroutine for the commercial finite elements (FE) software Abaqus/Standard and used for the prediction of the cyclic failure of lead-free solder materials, the crack formation in anisotropic AISI 316L steel specimens and the description of the failure behaviour of carbon steel notched round bars and flat grooved plates.

Keywords: Rate-dependent plasticity; Damage anisotropic evolution; Plastic anisotropy; Kinetic logarithmic spin; Hypoelastic-based plasticity

1. Introduction

Metal failure is a relevant topic in several industrial sectors (i.e. automotive, aerospace, civil infrastructures etc.), and its description has represented a challenge for many authors. The interest and increased attention to the topic can be justified by several aspects: the improvement of the design of components or structures to reduce the costs of production or maintenance; research on new construction or design strategies to introduce solutions that are innovative when compared to traditional approaches; the introduction of new materials or technologies that have broadened the field of the application of ductile materials (biomedical, aerospace, robotic etc.); better understanding the physically based mechanism of the damaging process to develop better numerical tools for a more realistic simulation of the process. In particular, this last aspect became particularly relevant with the increase of the computational power and the advent of finite elements (FE), extended finite elements (X-FE), discrete elements (DE) methods etc. The ability to push the computation limits with more accurate meshes, geometries and complex loading or boundary conditions has led to the development of sophisticated constitutive models and damage criteria.

The phenomenon of material failure can be the outcome of very different processes, such as ductile fracture, low ductility fracture and progressive failure mechanism (i.e. fatigue or creep). An exhaustive description of the

* Corresponding authors.
E-mail addresses: fincato@jwri.osaka-u.ac.jp (R. Fincato), tsutsumi@jwri.osaka-u.ac.jp (S. Tsutsumi).

https://doi.org/10.1016/j.cma.2021.114165
0045-7825/

aforementioned mechanisms can be found in a recent work of Pantazopoulos [1] or the study by Besson et al. [2]. The present work focuses on ductile fracture where large plastic deformations are usually observed, which alter the geometry or shape of the structures or components (i.e. necking, shear bands and deformation localisation). The origin of the damaging process can be observed at a micro level [3–8], and it is generally triggered by the presence of internal material defects (e.g. voids and inclusions) around which a stress localisation induces crystallographic slips and progressive decohesion at the interface between the inclusion and the matrix. Alternatively, the inclusion can break under the effect of the surrounding stress fields. Several recent works (de Geus et al. [9]; Nguyen et al. [10]; Siddiq, [11]; Vajragupta et al. [12]; Zhao et al. [13]; among others) investigated the damage at a micro or mesoscale of observation by coupling crystal plasticity constitutive equations with scalar or tensorial damage variables. On the one hand, a micro or mesoscale approach is extremely useful for understanding the mechanism of void formation, growth and coalescence as well as the main role played by the matrix material anisotropy (either elastic or plastic), different crystallographic orientations, porosity etc. A macro scale of observation continues to be very useful from an industrial point of view, as it describes the damage as a progressive degradation of the mechanical properties of the material. Macroscopic damage models are usually divided into three categories [2,14,15]: empirical failure criteria [16–21], phenomenological models [22–29] and micromechanics-based models [30–34]. A discussion of the advantages and disadvantages of the different formulations is not the goal of the present work. A detailed discussion of the models can be found in Cao [35], while a comparison between different damage criteria and modelling strategies can be found in other studies [14,36–39].

Despite the different damage models derived by the empirical failure criteria and the phenomenological and micromechanics-based approaches, almost all the recent constitutive models [19,22,35,40–50] consider the damage evolution as a function of the inelastic strain and two non-dimensional stress parameters, i.e. the stress triaxiality and the Lode angle. In particular, damage evolution laws based on the two dimensionless stress parameters allow one to predict a realistic deformation at fracture under various loading conditions.

Recently, several efforts have been made to describe the anisotropic fracture, especially while considering anisotropic metal sheets. Badreddine et al. [48] developed a fully coupled elastoplastic and isotropic damage constitutive model at finite strains, which considers plastic-induced anisotropy by the distortion of the yield surface. The model results were in good agreement with the experimental results obtained by Khan et al. [51] for the aluminium alloy AL1100. In the studies by Badreddine et al. [52] and Badreddine and Saanouni [48], the authors developed a non-associative finite strain anisotropic elastoplastic model fully coupled with anisotropic ductile damage. The damage was described by a second-order tensor and the coupling with the plastic internal variables was realised by means of the equivalent energy principle. Rajhi et al. [53] applied a constitutive model that considered anisotropic ductile damage fully coupled with the anisotropic plastic flow to describe the anisotropic failure of 316L stainless steel. The numerical results showed good agreement with the experimental data, thereby pointing out the necessity of considering the anisotropy in the failure description of SS316L sheets. Recently, Zhang et al. [54] proposed an elastoplastic damage model by adopting a Hill48 yield criterion [55] and a scalar damage variable. The damage evolution accounted for the material anisotropy, Lode angle and stress triaxiality effects, resulting in a quite good description of the material failure of notched and flat-grooved AA7050-T7451 specimens. Habib et al. [56] investigated the anisotropic fracture of the ZEK100 magnesium alloy through experiments and numerical simulations and by considering different stress states and strain rate effects.

The goal of this study is to present a phenomenological coupled elasto-viscoplastic and damage model based on the constitutive equations of the Extended Overstress Subloading Surface (EOSS) theory [57,58] and developed within the framework of the *continuum damage mechanics* (CDM). The present model, named Damage Extended Overstress Subloading Surface (hereafter, DEOSS) model, aims to expand the previous fields of application of the Subloading Surface theory, and it considers time-dependent irreversible deformations, an anisotropic yield criterion (i.e. Hill48), anisotropic induced plasticity by means of a Chaboche's type kinematic hardening law [59] and a ductile damage evolution capable of taking into account a different damage evolution depending on the loading directions in relation to the axes of anisotropy. Based on the well-known Lemaitre's theory [60], a novel ductile damage evolution law is proposed, capable of considering the effect of the stress triaxiality, the Lode angle and the material anisotropy. Moreover, the constitutive equations are developed within a finite elastoplasticity framework under the assumption of hypoelastic-based plasticity using the *kinetic logarithmic spin* proposed by Jiao and Fish [61,62], thereby improving the description of the material deformation behaviour given in the previous works of the authors (e.g. [57,58,63–65]).

The paper is organised as follows: Section 2 introduces the constitutive equations of the coupled viscoplastic and damage model, dedicating an ad hoc session to the discussion of the damage evolution law and the kinematic framework. Section 3 deals with the numerical results in two parts. The first part aims to show the features of the novel damage evolution law, while the second reproduces certain experimental results found in the literature and certain experiments carried out by the authors in a previous work. Section 4 discusses the limitations that continue to persists in the current formulation of the model, leaving the investigation of such limitations to future works. Finally, the conclusions are presented in Section 5.

2. Constitutive equations

The constitutive equations are developed within a finite elastoplasticity framework under the assumption of hypoelastic-based plasticity. In detail, an Eulerian rate-type formulation is assumed where the constitutive laws are formulated in terms of objective rates of the Kirchhoff stress $\boldsymbol{\tau}$. Indicating the spatial coordinates of a generic material particle with $\mathbf{x}$ and its spatial velocity with $\mathbf{v}$, velocity gradient can be given as $\mathbf{L} = \partial\mathbf{v}/\partial\mathbf{x}$. Following the Cartesian decomposition, $\mathbf{L}$ can be decomposed into a symmetric part $\mathbf{D}$, i.e. the strain rate tensor, and a skew-symmetric part $\mathbf{W}$, which is the continuum spin. Thus,

$$\mathbf{D} = \left(\mathbf{L} + \mathbf{L}^T\right)/2; \quad \mathbf{W} = \left(\mathbf{L} - \mathbf{L}^T\right)/2. \tag{1}$$

The strain rate tensor $\mathbf{D}$ is additively decomposed into an elastic strain rate component $\mathbf{D}^{\mathrm{e}}$ and a viscoplastic strain rate component $\mathbf{D}^{vp}$:

$$\mathbf{D} = \mathbf{D}^{e} + \mathbf{D}^{vp}. \tag{2}$$

The stress power $\dot{p}$ can be written as:

$$\dot{p} = \boldsymbol{\tau}\colon \mathbf{D} = \boldsymbol{\tau}\colon \mathbf{D}^{e} + \boldsymbol{\tau}\colon \mathbf{D}^{p}. \tag{3}$$

where the Kirchhoff stress $\boldsymbol{\tau} = J\boldsymbol{\sigma}$ is defined as the product of the Cauchy stress $\boldsymbol{\sigma}$ and the determinant of the deformation gradient $J = \det(\boldsymbol{F})$. In this work negligible elastic volume changes and plastic incompressibility are considered (i.e., $J \approx 1$), therefore $\boldsymbol{\sigma} \approx \boldsymbol{\tau}$. In the following equations the Cauchy stress or its co-rotational rate will be adopted similarly to [66,67]. Moreover, a grade zero hypoelastic relation is assumed, adopting a elastic compliance tensor $\mathbf{E}^{-1}$ independent of the stress as in Jiao and Fish [61]. Isotropic elasticity is considered in this work, assuming that the plastic flow and plastic hardening have no effect on the elastic properties [27,48,67] and considering that elastic strains are generally small compared with plastic deformations in metallic materials. Moreover, the adoption of an isotropic elastic tensor simplifies the finite step integration of the constitutive equations as shown in the Appendix. This allows to define the elastic strain rate as $\mathbf{D}^{e} = \mathbf{E}^{-1}\colon \mathring{\tau} \approx \mathbf{E}^{-1}\colon \mathring{\boldsymbol{\sigma}}$. The symbol '$\circ$' indicates the co-rotational rate of the tensors, which is discussed in Section 2.3. The definition of the viscoplastic strain rate will be given in the following section.

2.1. Coupled elasto-viscoplastic and damage equations

The subloading surface (hereafter, SS) theory was formulated by Hashiguchi [68,69] in order to overcome the drawback of conventional plasticity theories regarding an abrupt formation of irreversible deformations whenever the stress state lies on the plastic potential during the loading process. The main feature of the SS theory is the addition of an internal variable, named the similarity centre $\mathbf{s}$ that moves in the stress space, following the evolution of the irreversible deformation and allowing a smooth generation of the plastic/viscoplastic strain. Since the initial formulation, several modifications were introduced to improve the material description. A detailed overview of the theory with several applications can be found in Hashiguchi [70].

The EOSS model was formulated by the authors Fincato and Tsutsumi [57,58] to improve the description of the time-dependent deformation of metallic materials under the cyclic loading condition that was still missing in the subloading surface theory. For sake of brevity, the constitutive equations of the EOSS model have been omitted here; the reader can refer to the aforementioned literature for a detailed explanation. The aim of the present work is to enrich the field of applications of the subloading surface theory to describe the failure behaviour of metals by considering plastic anisotropy. Therefore, this section deals with the coupling of anisotropic damage variables with

Table 1
State and associated variables in the DEOSS model.

	State variables	Associated state variables
Observable variables		
Elasticity	$\boldsymbol{\varepsilon}^{e}$	$\boldsymbol{\sigma}$
Internal variables		
Plasticity	$\boldsymbol{\varepsilon}^{vp}$	$\boldsymbol{\sigma}$
Similarity centre	$\boldsymbol{\varepsilon}^{vp}_{ss}$	$\mathbf{s}$
Kinematic hardening	$\boldsymbol{\varepsilon}^{vp}_{ks}$	$\boldsymbol{\alpha}$
Isotropic hardening	H	F
Isotropic damage	D	Y

the viscoplastic internal variables as well as the introduction of an anisotropic yield criterion. A summary of the constitutive equations is reported at the end of Section 2.2 (see Box 1).

Conventionally, two different configurations are considered in the CDM framework: (i) a damaged configuration that is characterised by the presence of defects and (ii) a mechanically equivalent fictitious undamaged configuration where the body does not present defects (cracks). In this work we assumed the so-called rotated frame formulation (RFF) [48,66,71,72] for expressing the constitutive laws in the actual damaged and fictitious undamaged configurations. Briefly, to fulfil the objectivity requirement the constitutive equations are expressed in local rotated configurations unaffected by any superposed spatial rigid body motion and this local configuration is obtained from the current one by means of a proper orthogonal rotation tensor. Details about the orthogonal rotation tensor are given in the Appendix.

In the case of isotropy, a scalar internal variable, i.e. the damage variable D, is used to model the presence and the evolution of irreversible defects during loading from an initial state $D = D_0$ to the final material failure $D = 1$. In most cases, an initial value of $D_0 = 0$ is assumed. In the case of anisotropy, the damage representation should be carried out with a tensorial variable, such as a set of vectors, second-order tensor [27,73,74] and fourth-order tensor [75,76] since the crack orientation and evolution are strongly influenced by the material microstructure. In this study, a scalar damage variable is considered; a discussion of the damage evolution is reported in Section 2.2. The starting point is the definition of the variables that characterise the failure phenomenon and the distinction of the variables into two classes: the observable variables and the internal variables (see Table 1).

The state variables $\boldsymbol{\varepsilon}^{vp}_{ss}$ and $\boldsymbol{\varepsilon}^{vp}_{ks}$ in Table 1 are objective Eulerian quantities that represent the storage viscoplastic strains associated with the similarity centre and the back stress, respectively. In particular, it is assumed that the sum of the storage strains (or the strain rates $\mathbf{D}^{vp}_{ss}$, $\mathbf{D}^{vp}_{ks}$) and the corresponding dissipative counterparts $\boldsymbol{\varepsilon}^{vp}_{sd}$ and $\boldsymbol{\varepsilon}^{vp}_{kd}$(or their rates $\mathbf{D}^{vp}_{sd}$, $\mathbf{D}^{vp}_{kd}$) additively form the total viscoplastic strain $\boldsymbol{\varepsilon}^{vp}$(or total viscoplastic strain rate $\mathbf{D}^{vp}$). A similar assumption was also formulated by Hashiguchi [70].

$$\begin{aligned} \boldsymbol{\varepsilon}^{vp} &= \boldsymbol{\varepsilon}^{vp}_{ss} + \boldsymbol{\varepsilon}^{vp}_{sd} \quad \mathbf{D}^{vp} = \mathbf{D}^{vp}_{ss} + \mathbf{D}^{vp}_{sd} \\ \boldsymbol{\varepsilon}^{vp} &= \boldsymbol{\varepsilon}^{vp}_{ks} + \boldsymbol{\varepsilon}^{vp}_{kd} \quad \mathbf{D}^{vp} = \mathbf{D}^{vp}_{ks} + \mathbf{D}^{vp}_{kd} \end{aligned} \tag{4}$$

The back stress variable $\boldsymbol{\alpha}$ is regarded as a linear combination of N non-linear independent kinematic hardening contributions $\boldsymbol{\alpha}_i$, following the approach proposed by Chaboche [59]. Each of the back stress $\boldsymbol{\alpha}_i$ is associated with the storage and dissipative parts of the viscoplastic strains (i.e. $\boldsymbol{\varepsilon}^{vp} = \boldsymbol{\varepsilon}^{vp}_{ks,i} + \boldsymbol{\varepsilon}^{vp}_{kd,i}$; $\mathbf{D}^{vp} = \mathbf{D}^{vp}_{ks,i} + \mathbf{D}^{vp}_{kd,i}$)

$$\boldsymbol{\alpha} = \sum_{i}^{N} \boldsymbol{\alpha}_i \quad i = 1, \dots N. \tag{5}$$

The state variables reported in Table 1 are organised in couples: the elastic strain and the Cauchy stress tensors $(\boldsymbol{\varepsilon}^{e}, \boldsymbol{\sigma})$; the viscoplastic strain and the Cauchy stress tensors $(\boldsymbol{\varepsilon}^{vp}, \boldsymbol{\sigma})$; the storage similarity centre viscoplastic strain and the similarity stress tensors $\left(\boldsymbol{\varepsilon}^{vp}_{ss}, \mathbf{s}\right)$; the storage kinematic hardening viscoplastic strain and the kinematic back stress tensors $\left(\boldsymbol{\varepsilon}^{vp}_{ks}, \boldsymbol{\alpha}\right)$; the isotropic hardening variable and the isotropic stress (H, F); the isotropic damage and the damage energy release rate (D, Y). Moreover, the *strain equivalence hypothesis* and the concept of *effective stress* [60] are here assumed, allowing to express the stress and strain quantities into the fictitious undamaged and the actual damaged configurations. The variables in the fictitious undamaged configuration are indicated with '$\sim$'.

$$\begin{gathered}\underset{\sim}{\boldsymbol{\sigma}}=\frac{\boldsymbol{\sigma}}{(1-D)};\quad \underset{\sim}{\boldsymbol{\alpha}}=\sum_i \underset{\sim}{\boldsymbol{\alpha}}_i=\frac{\boldsymbol{\alpha}}{(1-D)}=\sum_i \frac{\boldsymbol{\alpha}_i}{(1-D)};\quad \underset{\sim}{\mathbf{s}}=\frac{\mathbf{s}}{(1-D)};\quad \underset{\sim}{F}=\frac{F}{(1-D)}\\ \underset{\sim}{\boldsymbol{\varepsilon}}^e=\boldsymbol{\varepsilon}^e;\quad \underset{\sim}{\boldsymbol{\varepsilon}}^{vp}=\boldsymbol{\varepsilon}^{vp};\quad \underset{\sim}{H}=H;\end{gathered} \tag{6}$$

The variables defined in Eq. (6) are used in the state and dissipation potential expressed in the rotated fictitious undamaged configuration to derive the complete set of fully coupled constitutive equations. Firstly, the state potential is analysed while assuming the Helmholtz free energy ψ, which is written for an isothermal case and also assuming an additive decomposition of the potential in elastic-damage ψ_{ed} and plastic-damage ψ_{pd} terms. Further, it should be noted that the plastic-damage potential state can be additively decomposed into a kinematic ψ_{pk}, a similarity centre ψ_{ps} and isotropic ψ_{pi} terms. Alternative forms of state coupling are possible [77], depending on whether the damage affects the free energy associated with the plasticity ψ_{pd} or not.

$$\begin{gathered}\rho\psi=\rho\psi_{ed}\left(\boldsymbol{\varepsilon}^e,D\right)+\rho\psi_{pd}\left(\boldsymbol{\varepsilon}^{vp}_{ss},\boldsymbol{\varepsilon}^{vp}_{ks},H,D\right)=\rho\psi_{ed}\left(\boldsymbol{\varepsilon}^e,D\right)+\rho\psi_{pk}\left(\boldsymbol{\varepsilon}^{vp}_{ks},D\right)\\ +\rho\psi_{ps}\left(\boldsymbol{\varepsilon}^{vp}_{ss},D\right)+\rho\psi_{pi}\left(H,D\right)\\ \rho\psi_{ed}\left(\boldsymbol{\varepsilon}^e,D\right)=\frac{(1-D)}{2}\boldsymbol{\varepsilon}^e\colon\mathbf{E}^0\colon\boldsymbol{\varepsilon}^e\\ \rho\psi_{pk}\left(\boldsymbol{\varepsilon}^{vp}_{ks},D\right)=\sum_i\rho\psi_{pk,i}\left(\boldsymbol{\varepsilon}^{vp}_{ks},D\right)=(1-D)\sum_i\frac{1}{3}C_i\left(\boldsymbol{\varepsilon}^{vp}_{ks,i}\colon\boldsymbol{\varepsilon}^{vp}_{ks,i}\right)\\ \rho\psi_{ps}\left(\boldsymbol{\varepsilon}^{vp}_{ss},D\right)=(1-D)\frac{1}{2}c_s\boldsymbol{\varepsilon}^{vp}_{ss}\colon\boldsymbol{\varepsilon}^{vp}_{ss}\\ \rho\psi_{pi}\left(H,D\right)=(1-D)F_0\left[h_1H+\frac{h_1}{h_2}\exp\left(-h_2H\right)\right]\end{gathered} \tag{7}$$

where $\mathbf{E}^0$ is a fourth-order elasticity tensor (isotropic elasticity is assumed) in the fictitious undamaged configuration, F_0 is the initial yield stress, h_1 and h_2 are two material constants regulating the isotropic hardening, C_i is a material constant regulating the kinematic hardening and c_s is a material parameter regulating the movement of the similarity centre.

Sufficient conditions that are required for the Clausius–Duhem inequality (Eq. $(8)_1$) to hold are the elasticity law in Eq. $(8)_2$ together with the dissipation inequality in Eq. $(8)_3$ (i.e. ϕ_d mechanical dissipation).

$$\begin{gathered}\boldsymbol{\sigma}\colon\left(\mathbf{D}^e+\mathbf{D}^{vp}\right)-\rho\dot{\psi}_{ed}\left(\mathbf{D}^e,D\right)-\rho\dot{\psi}_{pk}\left(\mathbf{D}^{vp}_{ks},D\right)-\rho\dot{\psi}_{ps}\left(\mathbf{D}^{vp}_{ss},D\right)-\rho\dot{\psi}_{pi}\left(H,D\right)\geq 0\\ \boldsymbol{\sigma}=\rho\frac{\partial\psi_{ed}\left(\boldsymbol{\varepsilon}^e,D\right)}{\partial\boldsymbol{\varepsilon}^e}=(1-D)\,\mathbf{E}^0\colon\boldsymbol{\varepsilon}^e\\ \phi_d=\phi_{dp}+\phi_{dd}=\underbrace{\boldsymbol{\sigma}\colon\mathbf{D}^{vp}-\boldsymbol{\alpha}\colon\mathbf{D}^{vp}_{ks}-\mathbf{s}\colon\mathbf{D}^{vp}_{ss}-\dot{F}r}_{\text{viscoplastic dissipation }(\phi_{dp})}\quad\underbrace{-Y\dot{D}}_{\text{damage dissipation }(\phi_{dd})}\geq 0\end{gathered} \tag{8}$$

The associated state variables $\boldsymbol{\alpha}$, $\mathbf{s}$, F and Y in Eq. $(8)_3$ are defined as follows:

$$\begin{gathered}\boldsymbol{\alpha}=\rho\frac{\partial\psi_{pdk}\left(\boldsymbol{\varepsilon}^{vp}_{ks},D\right)}{\partial\boldsymbol{\varepsilon}^{vp}_{ks}}=(1-D)\frac{2}{3}C\;\;\boldsymbol{\varepsilon}^{vp}_{ks}=\sum_i(1-D)\frac{2}{3}C_i\;\;\boldsymbol{\varepsilon}^{vp}_{ks,i}\\ \mathbf{s}=\rho\frac{\partial\psi_{pdk}\left(\boldsymbol{\varepsilon}^{vp}_{ss},D\right)}{\partial\boldsymbol{\varepsilon}^{vp}_{ss}}=(1-D)\,c_s\boldsymbol{\varepsilon}^{vp}_{ss}\\ F=\rho\frac{\partial\psi_{pdi}\left(H,D\right)}{\partial r}=(1-D)\,F_0h_1\left[1-\exp\left(-h_2H\right)\right]\\ Y=Y_e+Y_k+Y_s+Y_i=\rho\frac{\partial\psi_{ed}\left(\boldsymbol{\varepsilon}^e,D\right)}{\partial D}+\rho\frac{\partial\psi_{pk}\left(\boldsymbol{\varepsilon}^{vp}_{ks},D\right)}{\partial D}+\rho\frac{\partial\psi_{ps}\left(\boldsymbol{\varepsilon}^{vp}_{ss},D\right)}{\partial D}+\frac{\partial\psi_{pi}\left(H,D\right)}{\partial D}\\ Y_e=\rho\frac{\partial\psi_{ed}\left(\boldsymbol{\varepsilon}^e,D\right)}{\partial D}=-\frac{1}{2}\boldsymbol{\varepsilon}^e\colon\mathbf{E}^0\colon\boldsymbol{\varepsilon}^e=-\frac{1}{2(1-D)^2}\boldsymbol{\sigma}\colon\left[\mathbf{E}^0\right]^{-1}\colon\boldsymbol{\sigma}\\ Y_k=\rho\frac{\partial\psi_{pdk}\left(\boldsymbol{\varepsilon}^{vp}_{ks},D\right)}{\partial D}=\sum_i\rho\frac{\partial\psi_{pk}\left(\boldsymbol{\varepsilon}^{vp}_{ks,i},D\right)}{\partial D}=-\sum_i\frac{1}{3}C_i\left(\boldsymbol{\varepsilon}^{vp}_{ks,i}\colon\boldsymbol{\varepsilon}^{vp}_{ks,i}\right)=-\sum_i\frac{3}{4}\frac{\boldsymbol{\alpha}\colon\boldsymbol{\alpha}}{\left[(1-D)^2C_i\right]}\\ Y_s=\rho\frac{\partial\psi_{pds}\left(\boldsymbol{\varepsilon}^{vp}_{ss},D\right)}{\partial D}=-\frac{1}{2}c_s\left(\boldsymbol{\varepsilon}^{vp}_{ss}\colon\boldsymbol{\varepsilon}^{vp}_{ss}\right)=-\frac{1}{2}\frac{\mathbf{s}\colon\mathbf{s}}{\left[(1-D)^2c_s\right]}\\ Y_i=\frac{\partial\psi_{pdi}\left(H,D\right)}{\partial D}=-F_0\left[h_1H+\frac{h_1}{h_2}\exp\left(-h_2H\right)\right]\end{gathered} \tag{9}$$

According to the previous formulation in the study by Fincato and Tsutsumi [57], the EOSS model is characterised by the following: the *dynamic loading surface*, which always passes through the current stress state $\boldsymbol{\sigma}$; the *normal-yield surface* that defines the plastic potential; the *subloading surface* that allows the generation of irreversible deformation in the so-called sub-yield domain. All the surfaces are related by means of a similarity transformation, and the centre of the similarity transformation is the similarity centre $\mathbf{s}$, which defines two similarity ratios R_d ($R_d > 0$) and R ($0 < \mathrm{R} < 1$). R_d expresses the ratio between the sizes of the dynamic loading and the normal-yield surface, while R defines the ratio between the sizes of the subloading and the normal-yield surface. Depending on the stress state and, therefore, the value assumed by R_d and R, the following nomenclature was proposed in the study by Fincato and Tsutsumi [57].

$$\begin{aligned} &R_d \leq 1 \quad and \quad R < 1 \quad \text{sub-yield stress state} \\ &R_d > 1 \quad and \quad R < 1 \quad \text{mix-stress state} \\ &R_d > 1 \quad and \quad R = 1 \quad \text{fully viscoplastic stress state} \end{aligned} \tag{10}$$

Referring to Fig. 1 the analytical definition of the surfaces in the undamaged configuration is reported here for the sake of completeness; a detailed discussion can be found in the aforementioned literature.

$$\begin{aligned} f\left(\hat{\underset{\sim}{\boldsymbol{\sigma}}}_y\right) &= \overline{F} \qquad normal-yield\ surface \\ f\left(\overline{\underset{\sim}{\boldsymbol{\sigma}}}\right) &= R_d\overline{F} \quad dynamic\ loading\ surface \\ f\left(\overline{\underset{\sim}{\boldsymbol{\sigma}}}_{ss}\right) &= R\overline{F} \qquad subloading\ surface \\ \overline{F} &= (F_0 + F) \\ \hat{\underset{\sim}{\mathbf{s}}} = \underset{\sim}{\mathbf{s}} - \underset{\sim}{\boldsymbol{\alpha}} \qquad \hat{\underset{\sim}{\boldsymbol{\sigma}}}_y &= \underset{\sim}{\boldsymbol{\sigma}}_y - \underset{\sim}{\boldsymbol{\alpha}} \end{aligned} \tag{11}$$

$$\underbrace{\begin{aligned} &\overline{\underset{\sim}{\boldsymbol{\sigma}}} = \underset{\sim}{\boldsymbol{\sigma}} - \overline{\underset{\sim}{\boldsymbol{\alpha}}} \quad \overline{\underset{\sim}{\boldsymbol{\alpha}}} = \underset{\sim}{\mathbf{s}} - R_d\,\hat{\underset{\sim}{\mathbf{s}}} \\ &\widetilde{\underset{\sim}{\boldsymbol{\sigma}}} = \underset{\sim}{\boldsymbol{\sigma}} - \mathbf{s} \\ &\overline{\underset{\sim}{\boldsymbol{\sigma}}}_{ss} = \underset{\sim}{\boldsymbol{\sigma}}_{ss} - \overline{\underset{\sim}{\boldsymbol{\alpha}}}_{ss} \quad \overline{\underset{\sim}{\boldsymbol{\alpha}}}_{ss} = \underset{\sim}{\mathbf{s}} - R\,\hat{\underset{\sim}{\mathbf{s}}} \end{aligned}}_{\text{sub-yield stress state}} \qquad \underbrace{\begin{aligned} &\overline{\underset{\sim}{\boldsymbol{\sigma}}} = \underset{\sim}{\boldsymbol{\sigma}} - \overline{\underset{\sim}{\boldsymbol{\alpha}}} \quad \overline{\underset{\sim}{\boldsymbol{\alpha}}} = \underset{\sim}{\boldsymbol{\alpha}} \\ &\overline{\underset{\sim}{\boldsymbol{\sigma}}}_{ss} = \underset{\sim}{\boldsymbol{\sigma}}_{ss} - \overline{\underset{\sim}{\boldsymbol{\alpha}}}_{ss} \quad \overline{\underset{\sim}{\boldsymbol{\alpha}}}_{ss} = \underset{\sim}{\mathbf{s}} - R\,\hat{\underset{\sim}{\mathbf{s}}} \end{aligned}}_{\text{mix stress state}} \qquad \underbrace{\begin{aligned} &\overline{\underset{\sim}{\boldsymbol{\sigma}}} = \underset{\sim}{\boldsymbol{\sigma}} - \overline{\underset{\sim}{\boldsymbol{\alpha}}} \quad \overline{\underset{\sim}{\boldsymbol{\alpha}}} = \underset{\sim}{\boldsymbol{\alpha}} \\ &\overline{\underset{\sim}{\boldsymbol{\sigma}}}_{ss} = \underset{\sim}{\boldsymbol{\sigma}}_{ss} - \overline{\underset{\sim}{\boldsymbol{\alpha}}}_{ss} \quad \overline{\underset{\sim}{\boldsymbol{\alpha}}}_{ss} = \underset{\sim}{\boldsymbol{\alpha}} \end{aligned}}_{\text{fully viscoplastic stress state}}$$

Similarly to the study by Hashiguchi [70], in this study, the expressions of the viscoplastic strain rate, the storage viscoplastic strain rates $\mathbf{D}^{vp}_{ks}$ and $\mathbf{D}^{vp}_{ss}$ sub loading $\dot{H}$ are obtained by assuming the existence of homogeneous positive and convex functions $g^p(\underset{\sim}{\boldsymbol{\sigma}})$, $g^k(\underset{\sim}{\boldsymbol{\alpha}})$, $g^s(\underset{\sim}{\mathbf{s}})$ and $g^F(\underset{\sim}{F})$ in the effective stress space. The definition of the homogeneous positive and convex function $g^D(Y)$ for the definition of the damage evolution is discussed in Section 2.2. The dynamic loading function f in Eq. (11)$_2$ is chosen for $g^p(\underset{\sim}{\boldsymbol{\sigma}})$ to obtain an associated flow rule for the definition of $\mathbf{D}^{vp}$ along the normalised outward normal $\overline{\mathbf{N}}$ to the viscoplastic potential.

$$\begin{aligned} \mathbf{D}^{vp} &= \frac{\partial g^p(\underset{\sim}{\boldsymbol{\sigma}})}{\partial \boldsymbol{\sigma}} = \frac{\partial f(\overline{\underset{\sim}{\boldsymbol{\sigma}}})}{\partial \boldsymbol{\sigma}} = \frac{\partial\left[\sqrt{3/2}\overline{\underset{\sim}{\boldsymbol{\sigma}}}\colon \mathbf{H}\colon \overline{\underset{\sim}{\boldsymbol{\sigma}}} - R_d\underset{\sim}{F}\right]}{\partial \boldsymbol{\sigma}} = \frac{\lambda}{(1-D)}\overline{\mathbf{N}}; \\ \mathbf{D}^{vp}_{ks,i} &= \mathbf{D}^{vp} - \mathbf{D}^{vp}_{kd,i} = \frac{\lambda}{(1-D)}\overline{\mathbf{N}} - \lambda\frac{\partial g^k(\underset{\sim}{\boldsymbol{\alpha}}_i)}{\partial \boldsymbol{\alpha}_i} \\ &= \frac{\lambda}{(1-D)}\overline{\mathbf{N}} - \frac{\lambda}{(1-D)}\sqrt{\frac{3}{2}}\frac{B_i}{C_i}\underset{\sim}{\boldsymbol{\alpha}}_i = \frac{\lambda}{(1-D)}\left(\overline{\mathbf{N}} - \sqrt{\frac{3}{2}}\frac{B_i}{C_i}\underset{\sim}{\boldsymbol{\alpha}}_i\right) \\ \mathbf{D}^{vp}_{ss} &= \mathbf{D}^{vp} - \mathbf{D}^{vp}_{sd} = \frac{\lambda}{(1-D)}\overline{\mathbf{N}} - \lambda\frac{\partial g^s(\underset{\sim}{\mathbf{s}})}{\partial \mathbf{s}} \\ &= \frac{\lambda}{(1-D)}\overline{\mathbf{N}} - \frac{\lambda}{(1-D)}\left\{\overline{\mathbf{N}} - \left(\frac{\chi}{R_d}\overline{\underset{\sim}{\boldsymbol{\sigma}}} - \hat{\underset{\sim}{\mathbf{s}}}\right) - \frac{1}{c_s}\left[\sum_i\left(C_i\overline{\mathbf{N}} - \sqrt{\frac{3}{2}}B_i\underset{\sim}{\boldsymbol{\alpha}}_i\right) + \frac{dF}{dH}\frac{1}{\underset{\sim}{F}}\hat{\underset{\sim}{\mathbf{s}}}\right]\right\} \\ \dot{H} &= -\lambda\frac{\partial g^F(\underset{\sim}{F})}{\partial F} = \sqrt{\frac{2}{3}}\frac{\lambda}{(1-D)} \\ \overline{\mathbf{N}} &= \frac{\overline{\underset{\sim}{\boldsymbol{\sigma}}}\colon \mathbf{H}}{\sqrt{\overline{\underset{\sim}{\boldsymbol{\sigma}}}\colon \mathbf{H}\colon \overline{\underset{\sim}{\boldsymbol{\sigma}}}}}\Big/\left|\frac{\overline{\underset{\sim}{\boldsymbol{\sigma}}}\colon \mathbf{H}}{\sqrt{\overline{\underset{\sim}{\boldsymbol{\sigma}}}\colon \mathbf{H}\colon \overline{\underset{\sim}{\boldsymbol{\sigma}}}}}\right| = \frac{\overline{\boldsymbol{\sigma}}\colon \mathbf{H}}{\sqrt{\overline{\boldsymbol{\sigma}}\colon \mathbf{H}\colon \overline{\boldsymbol{\sigma}}}}\Big/\left|\frac{\overline{\boldsymbol{\sigma}}\colon \mathbf{H}}{\sqrt{\overline{\boldsymbol{\sigma}}\colon \mathbf{H}\colon \overline{\boldsymbol{\sigma}}}}\right|; \quad \left|\overline{\mathbf{N}}\right| = 1 \end{aligned} \tag{12}$$

where λ is the viscoplastic multiplier and B_i are material constants defining the evolution of the back stresses. To account for the anisotropic behaviour of the plastic yielding, the second-order tensor $\mathbf{H}$ is introduced in Eq. (12),

according to the formulation proposed by Hill [55]. In particular, the present work considers the form reported in the study by De Borst and Feenstra [78]:

$$\mathbf{H} = \begin{bmatrix} \frac{1}{3}(H+G) & -\frac{1}{3}H & -\frac{1}{3}G & 0 & 0 & 0 \\ -\frac{1}{3}H & \frac{1}{3}(H+F) & -\frac{1}{3}F & 0 & 0 & 0 \\ -\frac{1}{3}G & -\frac{1}{3}F & \frac{1}{3}(F+G) & 0 & 0 & 0 \\ 0 & 0 & 0 & 2L & 0 & 0 \\ 0 & 0 & 0 & 0 & 2M & 0 \\ 0 & 0 & 0 & 0 & 0 & 2N \end{bmatrix}. \tag{13}$$

The material coefficients F, G, H, L, M, N can be determined experimentally. The isotropic von Mises yield criterion is recovered when all the parameters were set to unity. Lastly, the definition of the viscoplastic multiplier is given as in the study by Fincato and Tsutsumi [57]:

$$0 \leq \lambda = \frac{1}{\mu} \frac{\langle \exp\left[n\left(R_d - R\right)\right] - 1 \rangle}{\left(R_m - R_d\right)}, \tag{14}$$

where μ is the viscoplastic coefficient, n is the non-dimensional rate-sensitivity material constant and R_m is a material parameter limiting the maximum expansion of the dynamic loading surface (see Hashiguchi [70]). The definition of the viscoplastic strain rate and the storage viscoplastic strain rates $\mathbf{D}^{vp}_{ks}$ and $\mathbf{D}^{vp}_{ss}$ presented in Eq. (12) are used together with Eqs. $(8)_2$ and (9) to define the stress, back stress and similarity centre rates as follows:

$$\begin{aligned} \mathring{\boldsymbol{\sigma}} &= (1-D)\,\mathbf{E}^0 : \left(\mathbf{D} - \mathbf{D}^{vp}\right) \\ \mathring{\boldsymbol{\alpha}} &= \sum_i (1-D)\,\frac{2}{3} C_i \;\mathbf{D}^{vp}_{ks,i} = \sum_i \left(\frac{2}{3} C_i \overline{\mathbf{N}} - \sqrt{\frac{2}{3}} B_i \frac{\boldsymbol{\alpha}_i}{(1-D)} \right) \lambda \\ \mathring{\mathbf{s}} &= c_s \lambda \left(\frac{\chi}{R_d} \frac{\overline{\boldsymbol{\sigma}}}{(1-D)} - \frac{\hat{\mathbf{s}}}{(1-D)} \right) + \mathring{\boldsymbol{\alpha}} + \frac{dF}{dH} \frac{1}{\underset{\sim}{F}} \frac{\hat{\mathbf{s}}}{(1-D)} \lambda \end{aligned}. \tag{15}$$

It should be pointed out that the definitions of the tensor rates given in Eq. (15) are not the time derivatives of Eqs. $(8)_2$ and (9) as in the study by Lemaitre and Desmorat [79]. However, they lead to the fulfilment of the equalities expressed in Eq. (6). The symbol '$\circ$' is omitted on the strain rate tensors, however, to satisfy the frame invariance, and all the tensorial state variables need to be considered in a configuration unaffected by any superposed spatial rigid body motion.

Observing the definition of the variables given in Eqs. $(8)_2$, (9) and (12), it was found that the inequality of Eq. $(8)_3$ is satisfied if the damage dissipation is also positive. This implies a restriction on the choice of $\dot{D}$ that needs to be positive as shown in Section 2.2

2.2. The ductile damage evolution law

In the previous section, the coupling of the internal variable with the damage variable was discussed without dealing with the evolution of the damage itself during the deformation process. In particular, the choice of the positive homogeneous function $g^D(Y)$ was not given. However, it was highlighted that the damage rate $\dot{D}$ must be positive to fulfil the dissipation inequality in Eq. $(8)_3$.

Several experiments [46,80–83] were conducted to understand the failure mechanism and main factors influencing the damage evolution in terms of void growth and coalescence up to the formation of macroscopic cracks. From the experimental results, it was concluded that regardless of the adopted modelling approach (i.e. uncoupled models, phenomenological models and micromechanics-based models), the failure phenomenon is mostly affected by two dimensionless stress parameters, i.e. the stress triaxiality η and the Lode angle θ. The effect of the latter can be included by using the dimensionless parameter $\overline{\theta}\left(-1 \leq \overline{\theta} \leq 1\right)$. The limits for the Lode angle parameters are represented by uniaxial tensile and compressive loading conditions where $\overline{\theta}$ is equal to $+1$ and -1, respectively, and it assumes intermediate values for all the other loading conditions ($\overline{\theta} = 0$ under shear or plane strain conditions).

The early work of Lemaitre [24,60] provided a thermodynamically consistent framework where the damage evolution law is derived from a dissipation potential that includes the effect of the stress triaxiality. However, in a

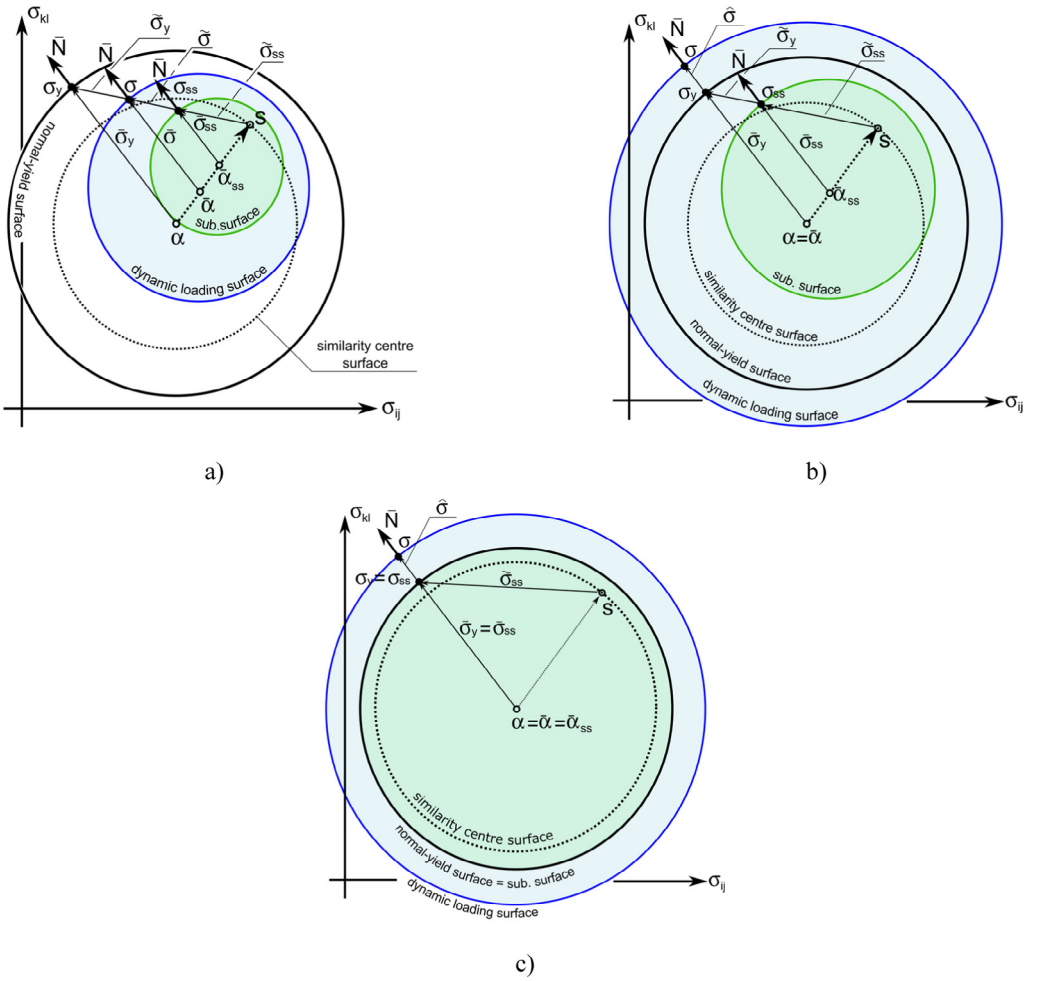

Fig. 1. Schematic representation of the subloading, dynamic-loading and normal-yield surface in the following: (a) sub-yield stress state during loading, (b) mix-stress state during loading and (c) fully viscoplastic stress state (Fig. 3 in Fincato and Tsutsumi [57]).

low-stress triaxiality regime, the Lemaitre model is sometimes unable to predict a realistic damage evolution due to the fact the failure phenomenon is mostly influenced by other factors, such as shear deformations. To overcome this drawback, recent models (e.g., Cao et al. [26]; Malcher and Mamiya, [84]; Mirone et al. [85], among others) included the effect of the Lode angle in the original Lemaitre's damage evolution law, thereby obtaining a good description of the failure even at shear-dominated low-stress triaxiality regimes. However, the damage description cannot account for anisotropy nor different damage evolution depending on the loading directions (i.e., the same damage evolution is obtained under similar loading conditions in different sextants of the deviatoric plane). For instance, the use a scalar multiplier function of the Lode angle parameter in Cao et al. [26] cannot differentiate the damage evolution under plane strain or shear conditions nor an evolution that depends on the direction of the load in relation to the axes of anisotropy.

To describe the anisotropic nature of the failure mechanism in metals, three main approaches have been developed in the literature [2,48]. The first one considers a set of vectors associated with predefined material directions (Costin, [86]; Rabotnov, [87]; among others). The second one uses a second-order damage tensor representation (Brünig, [88]; Desmorat and Cantournet, [89]; Murakami, [90]; among others), which offer the advantage of describing the actual state of the damage by symmetric second-order tensors. The third approach considers a fourth-order damage tensor (Chaboche, [91]; Ortiz, [92]; among others), and it leads to a consistent representation of the effective stress based on the strain equivalence assumption.

The current work aims to modify Lemaitre's damage evolution law by including the effects of the Lode angle and the definition of a multiplier factor that can diversify the damage evolution by considering the direction of the loading condition in relation to the axes of anisotropy. In particular, the purpose is to give a simple qualitative phenomenological scalar function that can result in a good description of the failure phenomenon and be used as a predictive tool in engineering applications. The damage evolution law is as follows:

$$
\begin{aligned}
&\dot{D} = \lambda \frac{\partial g^D(Y)}{\partial Y} = \sqrt{\frac{2}{3}} \frac{\lambda}{(1-D)} \left(-\frac{Y}{s_1}\right)^{s_2} \mathbf{n} : \mathbf{H}^D : \mathbf{n}; \quad \mathbf{n} = \frac{\overline{\boldsymbol{\sigma}}}{|\overline{\boldsymbol{\sigma}}|} \, |\mathbf{n}| = 1 \\
&\mathbf{H}^D = \begin{bmatrix}
1/3\left(G^D + H^D\right)\kappa & -1/3 H^D \kappa & -1/3 G^D \kappa & 0 & 0 & 0 \\
-1/3 H^D \kappa & 1/3\left(H^D + F^D\right)\kappa & -1/3 F^D \kappa & 0 & 0 & 0 \\
-1/3 G^D \kappa & -1/3 F^D \kappa & 1/3\left(G^D + F^D\right)\kappa & 0 & 0 & 0 \\
0 & 0 & 0 & 2L^D & 0 & 0 \\
0 & 0 & 0 & 0 & 2M^D & 0 \\
0 & 0 & 0 & 0 & 0 & 2N^D
\end{bmatrix}, \\
&\kappa = \overline{\theta}^2 + \left(1 - \overline{\theta}^2\right) b_1
\end{aligned}
\tag{16}
$$

where s_1 and s_2 are two material parameters with analogous meanings to those in the original Lemaitre's model and $\mathbf{n}$ is a normalised stress state introduced to take into account the directionality of the loading condition. It should be pointed out that $\mathbf{n}$ is a normalised tensor indicating the stress state in the deviatoric plane.$\mathbf{H}^D$ is a Hill-like tensor depending on six material parameters (F^D, G^D, H^D, L^D, M^D, $N^D > 0$), and κ is a scalar function of the material parameter b_1 and the Lode angle parameter $\overline{\theta}$ as defined in the studies by Tsutsumi et al. [19] and Zhang et al. [40]. It should be mentioned that the scalar function κ does not allow to model dissymmetric material response in tension and compression along the same loading direction. As seen in Eq. $(16)_1$, the novelty of the proposed damage evolution law lies in the scalar term $\mathbf{n} : \mathbf{H}^D : \mathbf{n}$, which is discussed in the following points:

- If the material parameters defining the Hill-like tensor $\mathbf{H}^D$ are positive, then the damage rate $\dot{D}$ is positive, thereby satisfying the requirement for the dissipation inequality.
- If the material parameters F^D, G^D, H^D, L^D, M^D, N^D and b_1 are to be unitary, then the original Lemaitre's law is recovered (since $|\mathbf{n}| = 1$), thereby allowing the failure description of the material to be influenced uniquely by the stress triaxiality.
- If $F^D = G^D = H^D = L^D = M^D = N^D = 1$ and $b_1 > 1$, the damaging process under plane strain conditions (i.e. $\overline{\theta} = 0$) can be enhanced in a manner similar to the enhanced Lemaitre's model proposed by Cao et al. [26]. Section 3.5 shows the effect of the b_1 parameter on the prediction of the failure behaviour of carbon construction steel round notched bars and flat grooved plates. The same set of numerical tests was performed in the study by Tsutsumi et al. [19] by adopting a Mohr–Coulomb failure criterion [16].
- The damage evolution varies depending on the material parameters F^D, G^D, H^D, L^D, M^D, N^D, b_1 and the stress state given by the unitary tensor $\mathbf{n}$. This allows one to take into consideration the tendency for damage to accumulate fast or slow, depending on the loading conditions. Section 3.4 reports the numerical results obtained in the failure description of the stainless steel 316L samples previously investigated by Rajhi et al. [53].
- The idea is to diversify the effect on the damage evolution induced by the normal and shear components of the stress. For instance, in the case of shear-dominated loading, the material parameters L^D, M^D, N^D can be set independently to enhance the damage evolution since the normal components of the unitary normal are negligible, as in the numerical example reported in Section 3.2. On the contrary, in the absence of shear components, the constants F^D, G^D, H^D and b_1 govern the damage evolution. These two sets of parameters should be calibrated in separate tests (i.e. tensile and shear tests).
- Depending on the deviatoric stress state, the term $\mathbf{n} : \mathbf{H}^D : \mathbf{n}$ affects the damage evolution uniquely. Therefore, the influence on the damage given by the stress triaxiality still depends on the damage energy release rate.

The following box summarises the constitutive equations of the DEOSS model. The computation of the similarity ratios R_d and R or the loading criterion is not discussed here. Details can be found in the study by Fincato and Tsutsumi [57].

- Viscoplastic split of the strain rate tensor

$$\mathbf{D} = \mathbf{D}^{e} + \mathbf{D}^{vp}.$$

- Linear elastic law (rate form)

$$\mathring{\boldsymbol{\sigma}} = (1-D)\,\mathbf{E}^{0}\colon \left(\mathbf{D} - \mathbf{D}^{vp}\right).$$

- Dynamic loading surface

$$f(\overline{\boldsymbol{\sigma}}) = \sqrt{3/2\overline{\boldsymbol{\sigma}}\colon \mathbf{H}\colon \overline{\boldsymbol{\sigma}}} - (1-D)\,R_d\underset{\sim}{\overline{F}}; \quad \underset{\sim}{\overline{F}} = (F_0 + \underset{\sim}{F}).$$

- Viscoplastic flow rule

$$\mathbf{D}^{vp} = \frac{1}{\mu(1-D)}\frac{\langle \exp\left[n\left(R_d - R\right)\right] - 1\rangle}{(R_m - R_d)}\overline{\mathbf{N}}; \quad \lambda = \frac{1}{\mu}\frac{\langle \exp\left[n\left(R_d - R\right)\right] - 1\rangle}{(R_m - R_d)}$$
$$\overline{\mathbf{N}} = \frac{\partial f(\overline{\boldsymbol{\sigma}})}{\partial \overline{\boldsymbol{\sigma}}}\Bigg/\left|\frac{\partial f(\overline{\boldsymbol{\sigma}})}{\partial \overline{\boldsymbol{\sigma}}}\right|; \quad \left|\overline{\mathbf{N}}\right| = 1$$

- Isotropic hardening law

$$\underset{\sim}{\overline{F}} = F_0\left[1 + h_1\left(1 - \exp\left(-h_2 H\right)\right)\right]; \quad H = \int_0^T \sqrt{\frac{2}{3}}\frac{\lambda}{(1-D)}dt, \quad t \in [0, T].$$

- Back stress and similarity centre rates

$$\mathring{\boldsymbol{\alpha}} = \sum_i (1-D)\,\frac{2}{3}C_i\ \mathbf{D}^{vp}_{ks,i} = \sum_i \left(\frac{2}{3}C_i\overline{\mathbf{N}} - \sqrt{\frac{2}{3}}B_i\frac{\boldsymbol{\alpha}_i}{(1-D)}\right)\lambda$$
$$\mathring{\mathbf{s}} = c_s\lambda\left(\frac{\chi}{R_d}\frac{\overline{\boldsymbol{\sigma}}}{(1-D)} - \frac{\hat{\mathbf{s}}}{(1-D)}\right) + \mathring{\boldsymbol{\alpha}} + \frac{dF}{dH}\frac{1}{\underset{\sim}{F}}\frac{\hat{\mathbf{s}}}{(1-D)}\lambda$$

- Damage evolution law and energy release rate

$$\dot{D} = \sqrt{\frac{2}{3}}\frac{\lambda}{(1-D)}\left(-\frac{Y}{s_1}\right)^{s_2}\mathbf{n}\colon \mathbf{H}^{D}\colon \mathbf{n}; \quad \mathbf{n} = \frac{\overline{\boldsymbol{\sigma}}}{|\overline{\boldsymbol{\sigma}}|}\,|\mathbf{n}| = 1$$
$$Y = Y_e + Y_k + Y_s + Y_i$$

- Similarity ratio R (viscoplastic loading process)

$$R = \frac{2}{\pi}(1-R_e)\cos^{-1}\left[\cos\left(\frac{\pi}{2}\frac{\langle R_0 - R_e\rangle}{1-R_e}\right)\exp\left(-\frac{\pi}{2}u\frac{H - H_0}{1-R_e}\right)\right] + R_e$$
$$H_0,\ R_0 \quad \text{initial conditions}$$

- Similarity ratios R_d and R (elastic unloading process)

$$R_d = \frac{\left(\tilde{\boldsymbol{\sigma}}\colon \mathbf{H}\colon \hat{\mathbf{s}}\right) + \sqrt{\left(\tilde{\boldsymbol{\sigma}}\colon \mathbf{H}\colon \hat{\mathbf{s}}\right)^2 + \left(\frac{2}{3}F^2 - \left(\hat{\mathbf{s}}\colon \mathbf{H}\colon \hat{\mathbf{s}}\right)\right)\left(\tilde{\boldsymbol{\sigma}}\colon \mathbf{H}\colon \tilde{\boldsymbol{\sigma}}\right)}}{\left(\frac{2}{3}(1-D)^2F^2 - \left(\hat{\mathbf{s}}\colon \mathbf{H}\colon \hat{\mathbf{s}}\right)\right)}$$
$$R = R_d$$

Box 1. Summary of the DEOSS constitutive model.

In Box 1, u is a material parameter regulating the amount of plastic deformation in the sub-yield and mix-stress states and R_e is a material parameter defined by Tsutsumi et al. [93] to introduce a small elastic domain for better modelling of the material behaviour ($R_e > 0.2$ usually for metals).

2.3. The co-rotational spin

The co-rotational Cauchy stress rate $\mathring{\boldsymbol{\sigma}}$ introduced in the previous section can be written as follows:

$$\mathring{\boldsymbol{\sigma}} = \dot{\boldsymbol{\sigma}} - \boldsymbol{\Omega}\boldsymbol{\sigma} + \boldsymbol{\sigma}\boldsymbol{\Omega}, \tag{17}$$

where $\boldsymbol{\sigma}$ is the second-order Cauchy stress tensor (negligible elastic volume changes and plastic incompressibility are assumed $\boldsymbol{\sigma} \approx \boldsymbol{\tau}$) and $\boldsymbol{\Omega}$ is a skew-symmetric second-order tensor, which is usually called the spin tensor. Hypoelastic-based plasticity with the additive decomposition of the strain rate has been adopted by several authors due to the simplicity of implementation in commercial finite element codes and the possibility of extending the constitutive equation of small deformation material models to finite strains, thereby defining a corotational framework. To obtain a description that is frame-invariant, extensive work has been carried out to define the appropriate co-rotational stress tensor in Eq. (17) by adopting several definitions of the spin tensor $\boldsymbol{\Omega}$.

Among the theoretically infinite choices [94], the Jaumann [95] and Green–Naghdi [96] stress rates have been frequently used in FE simulations for metallic materials. The Jaumann co-rotational stress rate has also been selected for the evaluation of the elastoplastic deformation of metals in the previous works of the authors (e.g. Fincato and Tsutsumi, [57,64]; Tsutsumi and Fincato, [19,97]). A comparison of the material description given by different stress rate definitions can be found in certain studies [98–101]. However, the models based on the additive decomposition of the strain rate tensors are known to suffer from several drawbacks, such as a non-unique definition of the elastic rate of deformation [102], the oscillation of the stress in simple shear if the Jaumann rate is adopted [72,103] or artificial elastic energy dissipation [104,105]. To overcome these shortcomings, a new co-rotational stress rate, i.e. the logarithmic stress rate, was proposed by Xiao et al. [106,107], and subsequently adopted by Zhu et al. [108]. Alternatively, hyperelastic-based plasticity models were formulated based on the slip theory of crystals [109] that assumes the deformation gradient as the product of elastic and plastic deformation gradients. The work published by Brepols et al. [66] offered an interesting comparison between hyperelastic-based plasticity formulation and hypoelastic-based plasticity algorithms that adopt the Jaumann, the Green–Naghdi and the logarithmic stress rates, respectively.

Despite the large numbers of models based on the logarithmic stress rate [108,110–113], two recent works by Jiao and Fish [61,62] pointed out how even the approach proposed by Xiao et al. [106] suffers from a "nonphysical energy dissipation during unloading processes after the yield", which is known as *unloading stress ratcheting*; they proposed a hypoelastic-based plasticity model based on the kinetic logarithmic spin [62] or the modified kinetic logarithmic spin [61] in the case of plastically induced anisotropy. The work of Jiao and Fish proved the equivalence between the multiplicative hyperelastic-based plasticity and the additive hypoelastic-based plasticity that uses the kinetic logarithmic stress rate.

The kinetic logarithmic stress rate defined by means of the kinetic logarithmic spin is also adopted in this work. The expression of the co-rotational rate of the Cauchy stress in Eq. $(17)_3$ can be written as follows:

$$\begin{aligned} \mathring{\boldsymbol{\sigma}}^{k\log} &= \dot{\boldsymbol{\sigma}} - \boldsymbol{\Omega}^{k\log}\boldsymbol{\sigma} + \boldsymbol{\sigma}\boldsymbol{\Omega}^{k\log} \\ \boldsymbol{\Omega}^{k\log} &= \left(\mathbf{W} - \mathbf{W}^{p}\right) - \overline{\mathbf{W}}^{k\log}\left(\mathbf{B}^{k}\left(\boldsymbol{\sigma}, D\right), \mathbf{D}\right), \\ \mathbf{W}^{p} &= \alpha\left[\boldsymbol{\sigma}\mathbf{D}^{p} - \mathbf{D}^{p}\boldsymbol{\sigma}\right] \end{aligned} \tag{18}$$

where $\mathring{\boldsymbol{\sigma}}^{k\log}$ is the co-rotational kinetic logarithmic stress rate, $\boldsymbol{\Omega}^{k\log}$ is the kinetic logarithmic spin, $\mathbf{W}$ is the continuum spin defined in Eq. $(1)_2$, $\mathbf{W}^{p}$ is the plastic spin tensor defined by means of the material constant α according to Zbib and Aifantis [114], $\overline{\mathbf{W}}^{k\log}$ is a skew-symmetric second-order tensor valued function dependent on the total strain rate $\mathbf{D}$ as well as on the kinetic left Cauchy–Green deformation tensor $\mathbf{B}^{k}$. Eq. (18) defines the spin with respect to the axes of anisotropy characterised by the material substructure in average terms, and it allows one to consider the eventual rotation induced during the loading. The concept of plastic spin was first introduced by Dafalias [115], and it has been widely adopted by many authors (Duchene et al. [116]; Hashiguchi, [70]; Jiao and Fish, [62]). It should be mentioned that a different formulation of the kinetic logarithmic spin, called *modified kinetic logarithmic spin*, was proposed by Jiao and Fish [61] to consider the effect of the strain-induced anisotropy without the introduction of the plastic spin tensor of Eq. (18). Instead, the aforementioned work proposed the use of a skew-symmetric second-order tensor whose contribution vanishes in the absence of kinematic hardening.

For details about the variables and functions in Eq. (18), the reader can refer to the studies by Jiao and Fish [61,62]. The definition of the kinetic left Cauchy–Green deformation tensor in the present work is also a

Table 2
Viscoplastic and damage material constants.

Elastic modulus	206 [GPa]
υ	0.3
h_1, h_2	7.5, 1.55
R_e	0.25
C, B	15 000 [MPa], 300
u	1500
c_s	200
χ	0.9
F_0	225 [MPa]
s_1, s_2	350 [MPa], 1.05
μ, n, R_m	50 [s], 1.0, 50

Table 3
Damage parameters for the $\boldsymbol{H}^D$ tensor.

Case	F^D	G^D	H^D	L^D	M^D	N^D	b_1
A	1	1	1	1	1	1	1
B	1	0.3	1	1	1	1	1
C	1	1	0.3	1	1	1	1
D	1	1	1	3	3	3	1
E	1	1	1	3	3	3	1.5
F	1	1	1	1	1	1	1.5

function of the damage D. Details can be found in the Appendix where the description of the incrementally objective integration algorithm of the DEOSS constitutive equations is given for the user subroutine UMAT (Abaqus).

3. Numerical calculations and results

The constitutive equations of the DEOSS model were implemented via user subroutine for the commercial code Abaqus (ver 6.14). The present section deals with the results obtained from numerical tests, and it is divided into two parts. The first part aims to show some examples to clarify the features of the novel damage evolution law (see Section 3.1) and proves the correct implementation of the algorithm in a simple shear test with rotation of the anisotropy axes (see Section 3.2). The second part numerically reproduces the experimental results obtained by Bonnaud and Gudmundson [117] on a lead-free solder material (see Section 3.3), those obtained by Rajhi et al. [53] on a 316L stainless steel (see Section 3.4) and the results obtained by Tsutsumi et al. [57] on a construction carbon steel (see Section 3.5). The analyses in Sections 3.4 and 3.5 consider a critical value D_c for the damage, after which the macro crack can be considered as formed. The additional term is used to avoid numerical problems due to the localisation of the damage and viscoplastic deformations as discussed in Section 4.

3.1. Tensile tests

For sake of simplicity, the numerical analyses were carried out on single hexahedral elements with reduced integration (C3D8R Abaqus elements), quasi-static loading conditions and an isotropic yield criterion (i.e. the Hill48 parameters are set to unity). Moreover, the material parameters were selected to be representative of generic carbon steel, and they are reported in Table 2. Two types of analyses were conducted by varying the damage material parameters F^D, G^D, H^D, L^D, M^D, N^D, b_1 for a total of 5 cases (i.e. A, B, C, D, E, F, see Table 3).

The first set of analyses considers a simple monotonic tensile test on a cubic element that is isostatically constrained. The Lode angle parameter $\overline{\theta}$was constantly unitary, so no effect could be induced by a modification of the b_1 constant. To verify the frame invariance to a superposed rigid body rotation, the analyses were carried out without (i.e. w/o R) and with a 45° rotation along the z-axis (i.e. w R), thereby imposing the same prescribed displacement condition on the top of the cube (see Fig. 2a and b). Case A considers an isotropic damage variable. Since all the damage coefficients were set to unity, the damage evolution is influenced only by the viscoplastic multiplier and the damage energy release rate Y without the influence of the loading direction by means of the

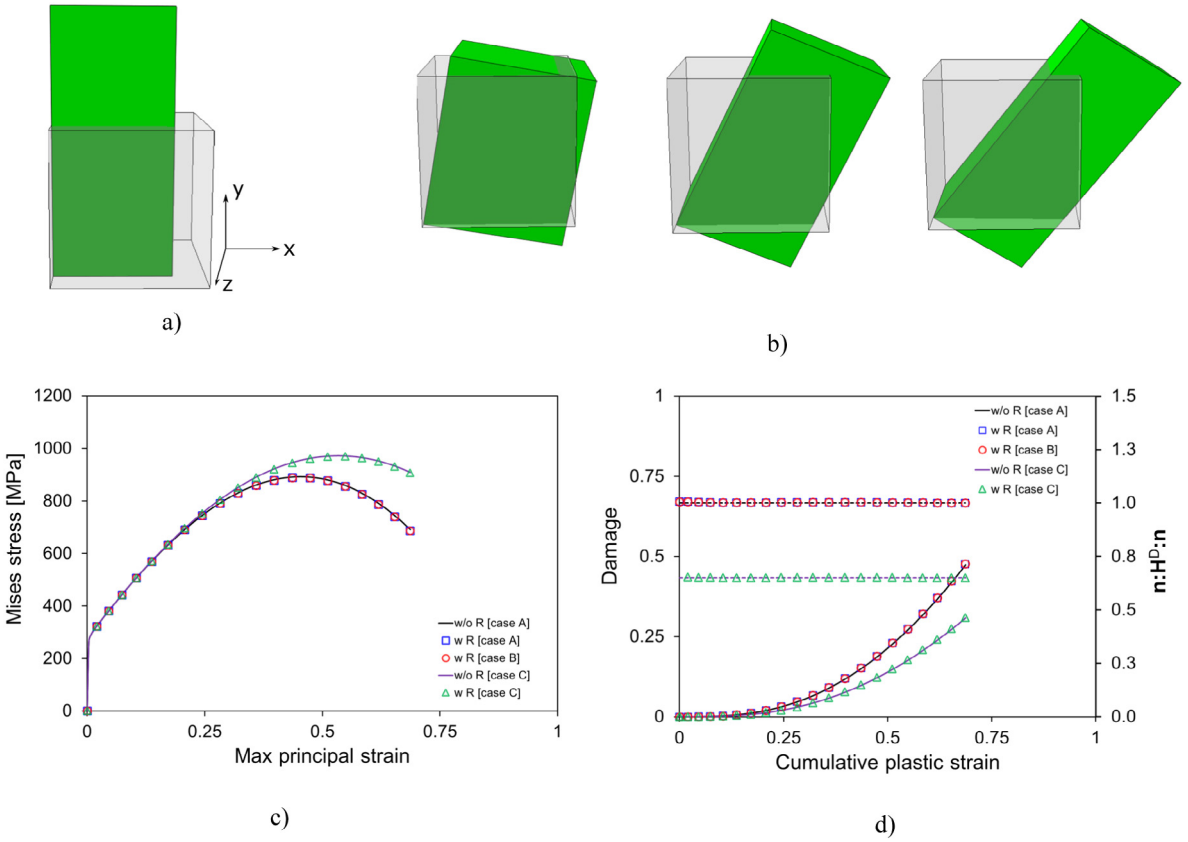

Fig. 2. (a) Tensile test without superposed rotation (w/o R), (b) Tensile test with 45° superposed rotation (w R), (c) Von Mises stress vs. max principal strain curves, (d) Damage and $\mathbf{n}:\mathbf{H}^D:\mathbf{n}$ evolutions vs. cumulative plastic strain H.

$\mathbf{n}:\mathbf{H}^D:\mathbf{n}$, which remained unitary. Moreover, the two solutions obtained with and without the superposed rigid body rotation overlap perfectly. A modification of the G^D parameter (i.e. case B) does not induce any modification in the damage evolution since G^D affects only the x and z components while the cube is still pulled along the y direction. On the contrary, after setting the parameter H^D to 0.3 (i.e. case C), the damage evolution is delayed since the term $\mathbf{n}:\mathbf{H}^D:\mathbf{n}$ constantly becomes $\sim$0.65 through the analysis. Once again, the superposition of a rigid body rotation did not alter the solution as evident from the perfect overlap between the solid purple line and the green triangle markers in Fig. 2c and d.

The second set of analyses considers a parallelepipedic shape element (the thickness was 0.1 for the other two sides). The base is constrained along the y-axis, the left vertical side is constrained along the x-axis, and the two faces perpendicular to the z-axis are constrained as well. Two uniform pressures of 500 MPa magnitude were applied in compression on the right side and in tension on top to generate a plane strain state. The Lode angle parameter $\overline{\theta}$ is constantly null during the loading.

This second set of analyses aims to show the role of the b_1 parameter; therefore, the constants F^D, G^D, H^D, affecting the normal components of the normal vector were set to a unitary value. Cases D and E in Fig. 3b and c show the different evolution of the Mises stress and damage under different values of the parameter b_1. As can be seen, the $\mathbf{n}:\mathbf{H}^D:\mathbf{n}$ scalar term assumes exactly the constant value of 1 and 1.5, respectively (see Fig. 3c). Due to the plane strain condition, the shear components of the stress do not affect the damage evolution as observed by comparing cases E and F where $b_1 = 1.5$, and the constants L^D, M^D, N^D were set to 3 and 1, respectively.

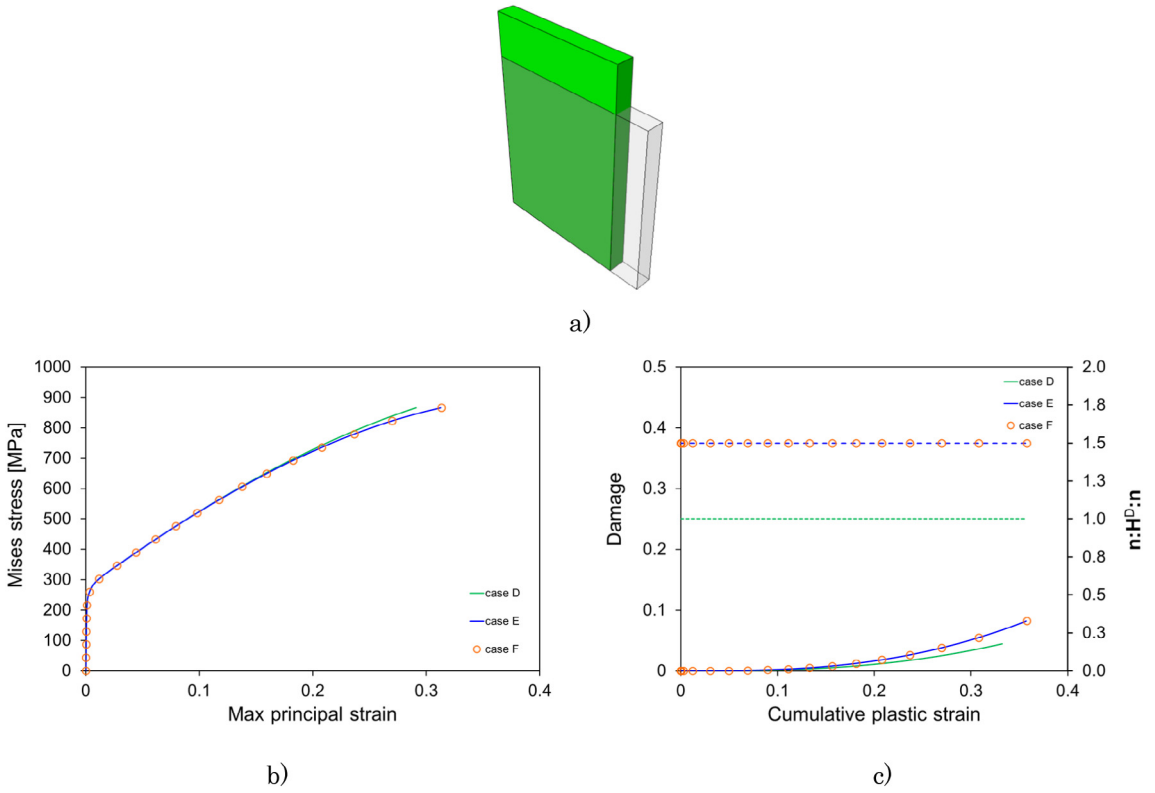

Fig. 3. (a) Sketch of the element deformation (b) Von Mises stress vs. max principal strain curves, (c) Damage and $\mathbf{n}:\mathbf{H}^{D}:\mathbf{n}$ evolutions vs. cumulative plastic strain H.

3.2. Simple shear

The purpose of this analysis is to show the ability of the DEOSS model to take into account the rotation of the anisotropy axes by reproducing the experimental results obtained by Duchene et al. [116]. As mentioned in Section 2.3, the kinetic logarithmic spin is defined with respect to the axis of anisotropy, and it allows one to consider the rotation of the substructure due to the loading conditions. This aspect is quite fundamental in FE simulations, as without the effect of the plastic spin, the Hill's yield criterion would be defined with respect to a reference system that does not follow the substructure rotation, leading to inaccurate results.

Duchene et al. [116] conducted a simple shear test on a low-carbon IF mild steel (FeP06t) rectangular sample (dimension $30 \times 3 \times 3$ mm) up to the shear strain $\gamma_{xy} = 70\%$, corresponding to an angle of about 35°. The loading rate was kept constant and equal to $\dot{\gamma}_{xy} = \sqrt{3}$ [s^{-1}]. The sample was obtained from a steel sheet produced by cold rolling and annealed. The measurement of the texture was conducted by X-ray diffraction technique at mid-thickness of the sheet at the initial and final stage of the load. Table 4 reports the material parameters adopted by Duchene et al. [116] in their numerical simulations as well as in the present study. Table 5 displays the Hill's coefficients of the steel sheet. This numerical example does not consider the effect of the damage. The following Eq. (19) reports the hardening law adopted and the function of the three material parameters K, ε_0 and n. The numerical simulations were conducted on a single hexahedral element with reduced integration (i.e. C3D8R Abaqus element) under simple shear loading conditions as shown by Duchene et al. [116].

$$F = K\,(\varepsilon_0 + H)^n \tag{19}$$

Fig. 4 displays the results of the numerical analyses conducted while considering an isotropic yield (i.e. von Mises criterion) and the Hill48 yield criterion. Moreover, in the case of material anisotropy, the importance of considering

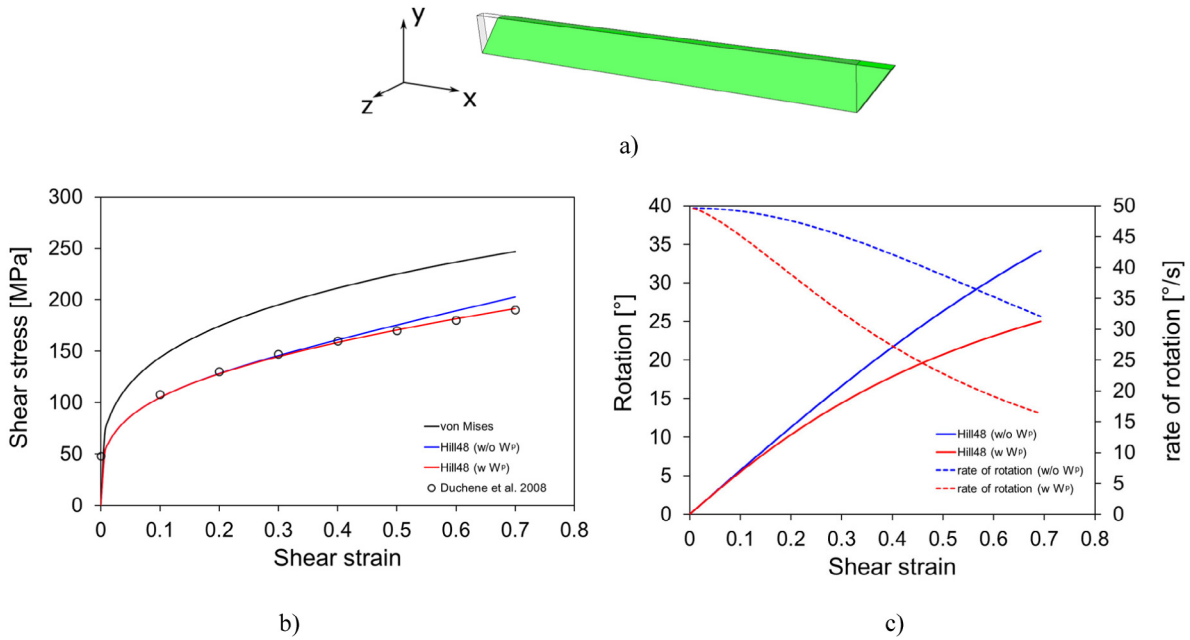

Fig. 4. Results on a single finite element. (a) Sketch of the sample and loading conditions (b) Shear stress vs. shear strain (*xy* components) (c) Rotation and rate of rotation of the axes of anisotropy (around the *z*-axis). (For interpretation of the references to colour in this figure legend, the reader is referred to the web version of this article.)

Table 4
FeP06t constants.

Elastic modulus	210 [GPa]
υ	0.3
K	550.3 [MPa]
ε_0	0.0011
N	0.278
$u,\ R_e$	1500, 0.7
C	200
χ	0.9
α	0.0065

Table 5
Hill's parameters of the steel sheet.

F	G	H	L	M	N
0.53	0.57	1.43	1.9	1.9	1.9

the contribution of the plastic spin in the definition of the co-rotational rate is described by the two solid blue and red curves in Fig. 4a. The formulation of $\mathbf{W}^{\mathrm{p}}$ requires the definition of the material constant α of Eq. $(18)_3$ that has been calibrated to overlap the experimental stress–strain curve.

The effect of the rotation generated by the plastic can be observed by plotting the rotation angle and the rate of rotation of the anisotropy axes against the shear strain as in Fig. 4c. The rotation angle and its rate refer to the *xy* component of the rotation tensor obtained by applying the exponential map to the kinetic logarithmic spin. The details about the procedure of defining the rotation tensor can be found in the Appendix. As it can be seen, the solution marked as 'w $\mathbf{W}^{\mathrm{p}}$' shows a higher decrease of the rotation angle compared to the solution 'w/o $\mathbf{W}^{\mathrm{p}}$'. This aspect is reflected in a smaller rotation of the anisotropy axes for the red solid curve with a final rotation angle of around 25°. It was observed that in case $\mathbf{W}^{\mathrm{p}}$ is neglected, the value of the final rotation coincides exactly with the rigid body rotation impressed during a simple shear test, which was 35° in this case. Experimentally, Duchene

Table 6
Elastoplastic and damage material constants.

Elastic modulus	195 [GPa]
υ	0.3
h_1, h_2	7.6, 1.5
R_e	0.99
C, B	7000 [MPa], 150
u	5000
F_0	300 [MPa]
α	0.04
s_1, s_2	530 [MPa], 1.0

Table 7
Hill's parameters.

F	G	H	L	M	N
0.922	0.894	1.1.106	1.4	1.5	1.5

Table 8
Damage parameters for the $\boldsymbol{H}^D$ tensor.

Case	F^D	G^D	H^D	L^D	M^D	N^D	b_1
G	1	1	1	1	1	1	1
H	5	3	2.5	1	4	6	1.5
I	1	1	1	2	1	1	1
L	5	3	2.5	2	4	6	1.5

et al. [116] measured a rotation of the substructure of around 27°, confirming the choice of the material constant α adopted in this simulation.

The following set of numerical analyses reproduces the simple shear numerical tests carried out by Badreddine et al. [67] (model 3 with $m = 4$ in Badreddine et al. [67]). The simulations were carried out in quasi-static loading conditions applying a simple shear displacement controlled loading condition on top of a hexahedral element with reduced integration (see Fig. 5). The displacement boundary condition was applied up to the shear strain $\gamma_{xy} = 100\%$. The material constants for the DEOSS model and the coefficients for the definition of the anisotropic Hill's tensor $\mathbf{H}$ were obtained from the referenced paper. The contribution of the similarity centre is neglected in this numerical example. The material constant α for the plastic spin was calibrated reproducing the shear stress–strain curve of the uncoupled solution reported in Badreddine et al. [67]. All the parameters are reported in Tables 6 and 7.

Four different analyses were carried out varying the coefficients of the $\mathbf{H}^{\mathrm{D}}$ tensor as reported in Table 8. Case G in Fig. 5b reports the stress–strain curves obtained considering a damage evolution where the damage parameters F^D, G^D, H^D, L^D, M^D, N^D, b_1 were set to unity to describe the analyses carried out in Badreddine et al. (2010). As it can be seen, the DEOSS is able to reproduce the same material result as in the referenced paper. It is worth mentioning that Badreddine et al. conducted the analyses by means of the commercial software Abaqus/Explicit with element deletion feature that allows to model a drop in stress around 100% shear strain. The present work does not consider this aspect, however, the purpose of the analyses is to show the ability of the DEOSS to control the damage evolution depending on the shear loading condition.

Subsequently, the damage coefficients were changed in case H with the exception of the parameter L^D to prove the invariance of the model response. As it can be seen, case G and H report the same stress–strain evolutions. This aspect is justified by the multiplier $\mathbf{n} : \mathbf{H}^D : \mathbf{n}$ in Fig. 5c that assumes a constant unitary value in both the analyses. As mentioned in Section 2.2, the formulation in Eq. (16) allows to diversify the damage evolution induced by shear stress independently from the normal components of the stress tensor. In a simple shear load on the xy plane, the damage evolution can be delayed (i.e., $0 \leq L^D < 1$) or accelerated (i.e., $L^D > 1$) by modifying the values of the L^D coefficient in $\mathbf{H}^{\mathrm{D}}$. For instance, case I and L show that the damage evolution could be accelerated by setting $L^D = 2$, remaining independent from the other damage parameters.

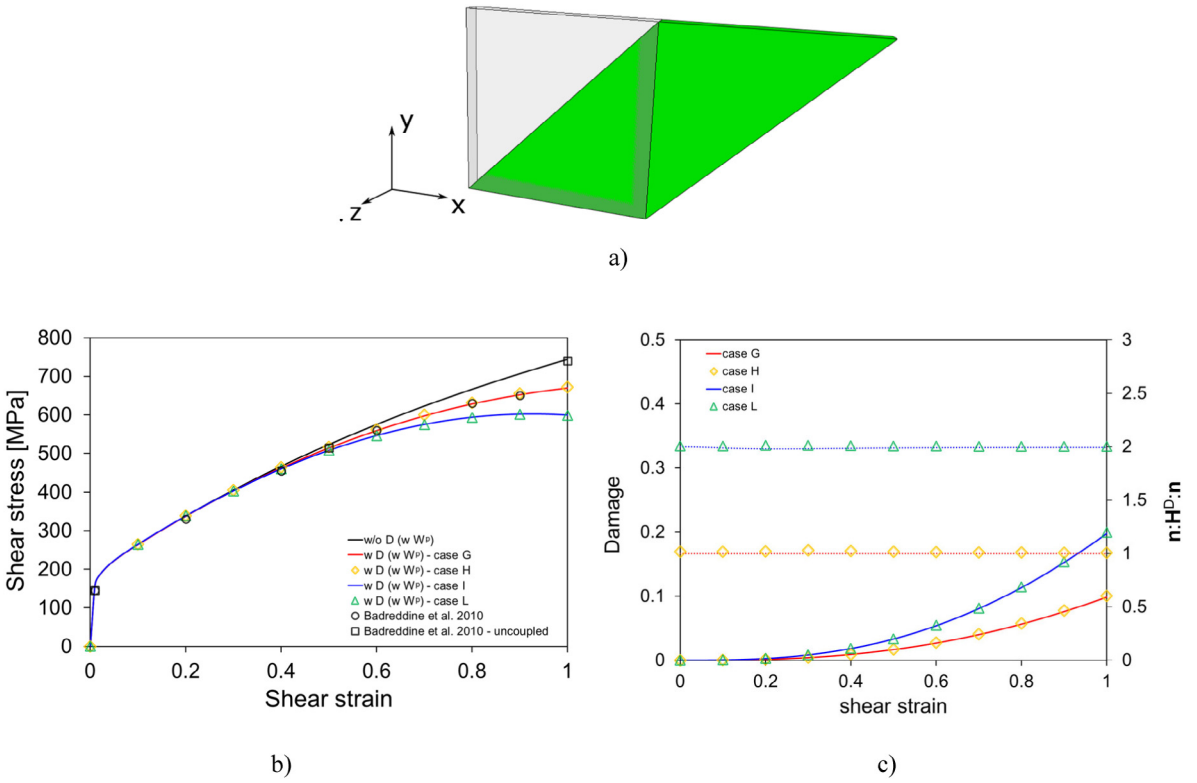

Fig. 5. Results on a single finite element. (a) Sketch of the sample and loading conditions (b) Shear stress vs. shear strain (*xy* components) (c) Damage and $\mathbf{n}:\mathbf{H}^{D}:\mathbf{n}$ evolution.

3.3. Cyclic loading on rate-dependent lead-free solder material

Bonnaud and Gudmundson [117] conducted a series of tests on lead-free solder round bars to investigate the strain rate sensitivity and the damaging mechanism of the material. The same set of experiments was reproduced numerically by Khoei and Eghbalian [118] by adopting a viscoplastic and damage model and implementing Lemaitre's damage evolution law. A previous work of the authors Fincato and Tsutsumi [58] showed the ability of the EOSS model to capture the strain rate dependency of the material; however, the damaging behaviour was not considered. The present work reproduces the cyclic loading analyses to characterise the progressive degradation of the mechanical properties. Briefly, Bonnaud and Gudmundson [117] conducted three monotonic tensile tests at different strain rates 0.2 [s^{-1}], 1 [s^{-1}] and 5 [s^{-1}] and a fully reversed cyclic loading condition at 1 [s^{-1}] strain rate for a total of 50 loading cycles. The round smooth bar was obtained from row cast bars, which were neither rolled nor extruded to keep the microstructure unaltered; so, the von Mises yield criterion was adopted for the numerical simulations. The details of the geometry and the mesh adopted can be found in the study by Fincato and Tsutsumi [58]. The elasto-viscoplastic parameters of the EOSS model have been discussed previously; they were adopted in this study and are presented in Table 9.

Due to the assumption of the isotropic plastic potential, the constants for the $\mathbf{H}^{D}$ tensor were set to unity. It should also be pointed out that the lack of variation in loading direction during the experiments does not allow to characterise the anisotropic behaviour of the damage. The details of the mesh and boundary conditions can be found in the study by Fincato and Tsutsumi [58]. The only parameters calibrated for the damage were s_1 and s_2, which were obtained to minimise the difference between the experimental and numerical stress–strain curves in the first two and the 50th cycles (only experimental data available). Figs. 6a and 5b report the numerical results for the monotonic tensile tests under three different loading rates as well as the first two cycles of the fully reversed cyclic loading analysis. The blue solid lines in Fig. 6b, c and d indicate the solution carried out with the EOSS

Table 9
Viscoplastic and damage material constants for the lead-free solder material.

Elastic modulus	15 [GPa]
υ	0.36
h_1, h_2	0.48, 5.5
R_e	0.2
C_1, B_1	9500 [MPa], 1400
C_2, B_2	210 [MPa], 6.5
u	800
F_0	40 [MPa]
s_1, s_2	340 [MPa], 1.05
μ, n, R_m	1.25 [s], 7.9, 27
c_s	50
χ	0.8

model, without the damage effect. The DEOSS result seems to be in good agreement with the experimental data and improves the material description given by Khoei and Eghbalian [118]. Even though the description of the damaging phenomenon given by Khoei and Eghbalian's model can be considered already satisfactory in this numerical example, it is important to highlight some general aspects to justify the adoption of the DEOSS theory with a larger number of material parameters. Firstly, Khoei and Eghbalian's model cannot predict a smooth development of plastic deformation in the sub-yield domain, as evident in the first three loading cycles of Fig. 6b. In particular, the smooth generation of inelastic strain predicted by the DEOSS theory assumes a critical role in describing the material ratcheting, and therefore damaging, in unidirectional cyclic loading conditions or cyclic loading conditions in the neighbourhood of the macroscopic yield stress [58,65,70]. Moreover, in general, the theory developed in [118] cannot consider plastic anisotropy, it is developed within an infinitesimal strain framework and it takes into account the contribution of a single non-linear back stress law. Here, five additional parameters had to be calibrated with the DEOSS model, due to an additional non-linear back stress contribution, the movement of the similarity centre and one material constant required for the definition of the viscoplastic multiplier (i.e. R_m).

The nominal stress vs. nominal strain curves for all the 50 loading cycles are reported in Fig. 6c for both the EOSS and DEOSS models. The EOSS model shows an increasing hardening behaviour through cycles that tends to saturate at around ± 80 MPa, while the viscoplastic and damage analyses results in an initial hardening, which is followed by softening induced by the damage.

Fig. 6d provides a detailed comparison of the experimental results and the numerical curves obtained by Khoei and Eghbalian [118] and by the DEOSS model. The experimental data shows a much stiffer elastic response during the elastic unloading. Overall, however, the tensile and compressive peaks are described quite well by the current model. Lastly, Fig. 6e displays the tensile and compressive peaks through cycles, showing the initial hardening followed by a linear softening. Lastly, it should be pointed out that the present form of the ductile damage evolution law in Eq. (16) does not consider the microcracks closure effect; therefore, the damage evolves in the same manner both in tension and compression. This aspect will be discussed later on, and it will be considered for the future development of the theory.

3.4. Anisotropic behaviour of SS316L stainless steel

The set of analyses discussed in this section deals with the anisotropic behaviour of 316L stainless steel samples under monotonic tensile loading conditions. Rajhi et al. [53] conducted a series of experiments and numerical analyses to characterise the damaging behaviour of specimens obtained from a rolled large sheet. To characterise the anisotropic behaviour, the tensile tests were conducted on specimens cut along three different directions: the rolling direction (hereafter, RD), along the direction transversal to the rolling process (hereafter, TD), and along the direction forming an angle of 45° degree with respect to the RD (hereafter, 45°) (see the sketch in Fig. 7). All the experiments were carried out by applying a displacement loading condition on one side of the sample with a 3 mm/s speed while keeping the opposite side constrained. The geometry of the samples (see Rajhi et al. [53] for the dimensions) was modelled with 3559 hexahedral elements with reduced integration (i.e. C3D8R Abaqus elements). A mesh refinement was adopted in the central part of the specimen.

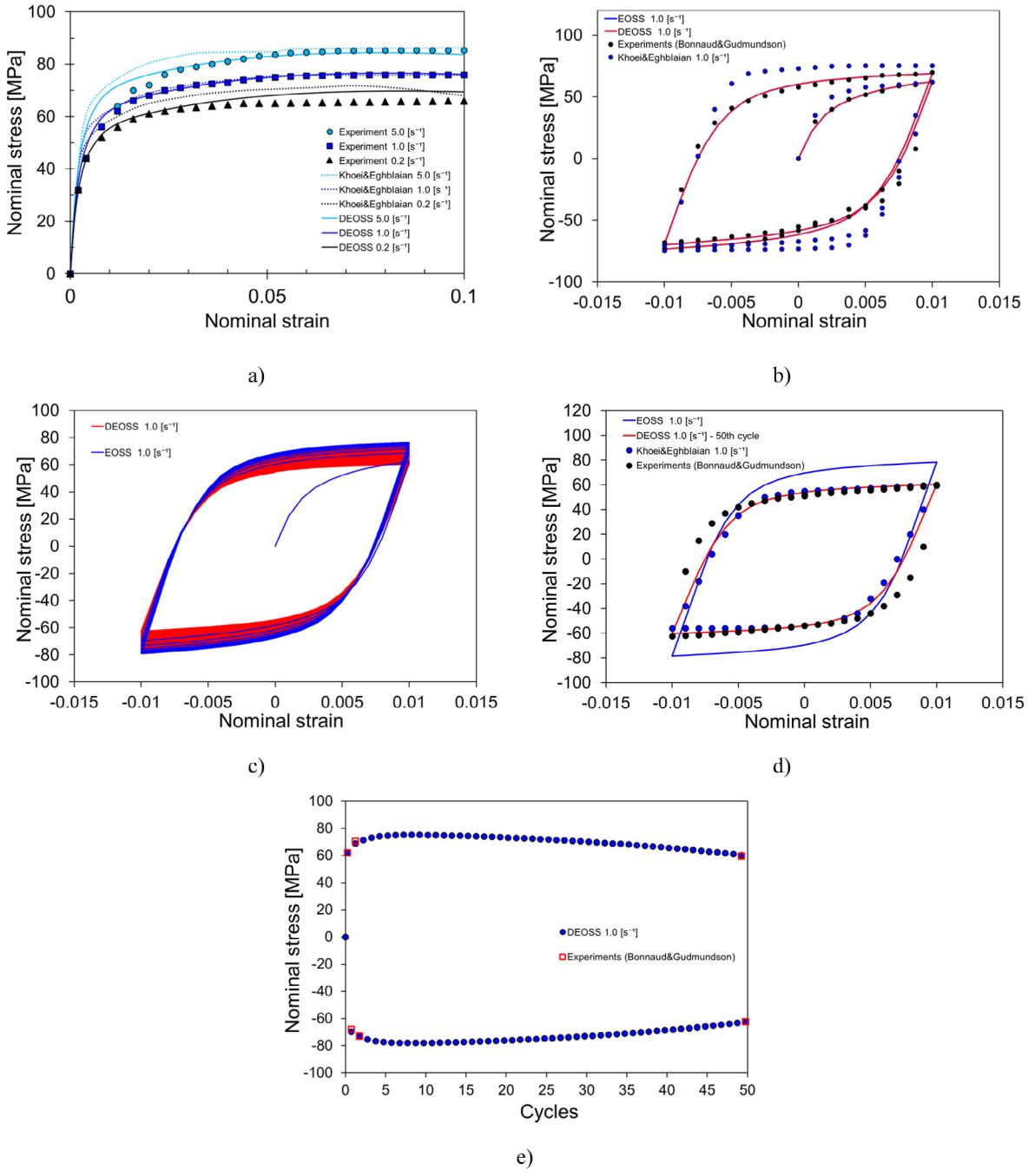

Fig. 6. (a) Nominal stress vs. nominal strain for the monotonic tensile tests under three different loadings rates, (a) fully reversed cyclic loading stress–strain curves for the 1 [s^{-1}] strain rate condition, (b) first two cycles, (c) all cycles (50 cycles), (d) 50th cycle, (e) envelope of the tensile and compressive peaks against cycles. (For interpretation of the references to colour in this figure legend, the reader is referred to the web version of this article.)

The simulation considers the same material parameters adopted by Rajhi et al. [53] as reported in Table 10. In addition, the material parameters R_e, u, proper of the DEOSS and the viscoplastic parameters μ, n and R_m were calibrated to fit the experimental stress and strain curves. Since the analyses are limited to monotonic tensile tests

Table 10
Viscoplastic and damage material constants for the 316L steel.

Elastic modulus	200 [GPa]
υ	0.3
h_1, h_2	7.25, 1.475
R_e	0.25
C_1, B_1	15 000 [MPa], 300
u	1500
F_0	225 [MPa]
s_1, s_2	140 [MPa], 1.0
μ, n, R_m	1.75 [s], 25, 20
D_c	0.2

Table 11
Hill's parameters of the 316L steel sheet.

F	G	H	L	M	N
1.60	1.52	0.48	1.025	1.0	1.0

Table 12
Parameters for the damage multiplier $\mathbf{n}:\mathbf{H}^D:\mathbf{n}$.

F^D	G^D	H^D	L^D	M^D	N^D	b_1
0.3	1	1	1	1	1	1

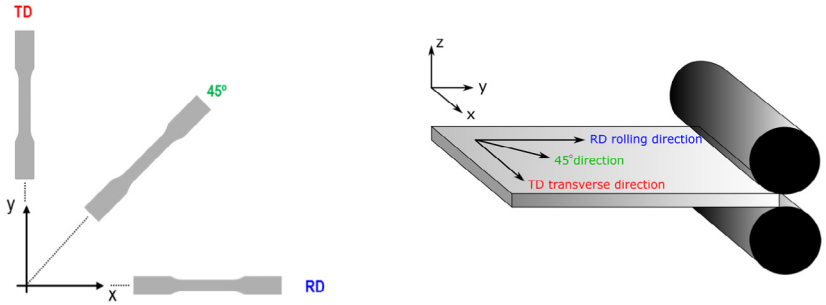

Fig. 7. Sketch of the specimens with respect to the reference system.

the constant c_s was set to 0, neglecting the effect of the similarity centre. Moreover, Rajhi et al. [53] reported the Hill48 parameters displayed in Table 11. The calibration of the damage parameters for the tensor $\mathbf{H}^D$ was conducted by assuming the failure behaviour of the RD specimen as a reference and setting G^D and H^D to unity; subsequently, the coefficient F^D was calibrated by running the tensile simulation for the specimen TD to achieve the experimental final displacement to failure. The components L^D, N^D, M^D and b_1 were assumed as unitary since they play a secondary role in uniaxial tensile loading conditions. The validation of the set of parameters was conducted on the specimen 45°. It should be pointed out that due to the lack of experimental data, the constants in Table 12 are not the only possible choice, since a proper description of the material failure behaviour needs to be obtained by performing additional tests, for instance, with different loading conditions (a tensile test along the z-axis and shear tests) or by adopting different geometries for the samples (flat grooved plates to investigate the plane strain conditions and the role of the b_1). However, the choice of the constants provides a good description of the material under tensile loading conditions on the xy plane of anisotropy.

Fig. 8a reports the experimental (round solid markers) and numerical (solid lines) force vs. displacement curves. Overall, the simulations seem to be in good agreement with the experimental data in terms of force–displacement trends and final displacement to failure. As mentioned earlier, the constants G^D and H^D are unitary, so the $\mathbf{n}:\mathbf{H}^D:\mathbf{n}$ multiplier keeps a constant unitary value during the simulation (see blue line in Fig. 8c). F^D was set to 0.3 to catch a 'delayed' material failure along the TD direction. The term $\mathbf{n}:\mathbf{H}^D:\mathbf{n}$ in Fig. 8c assumes almost a constant value

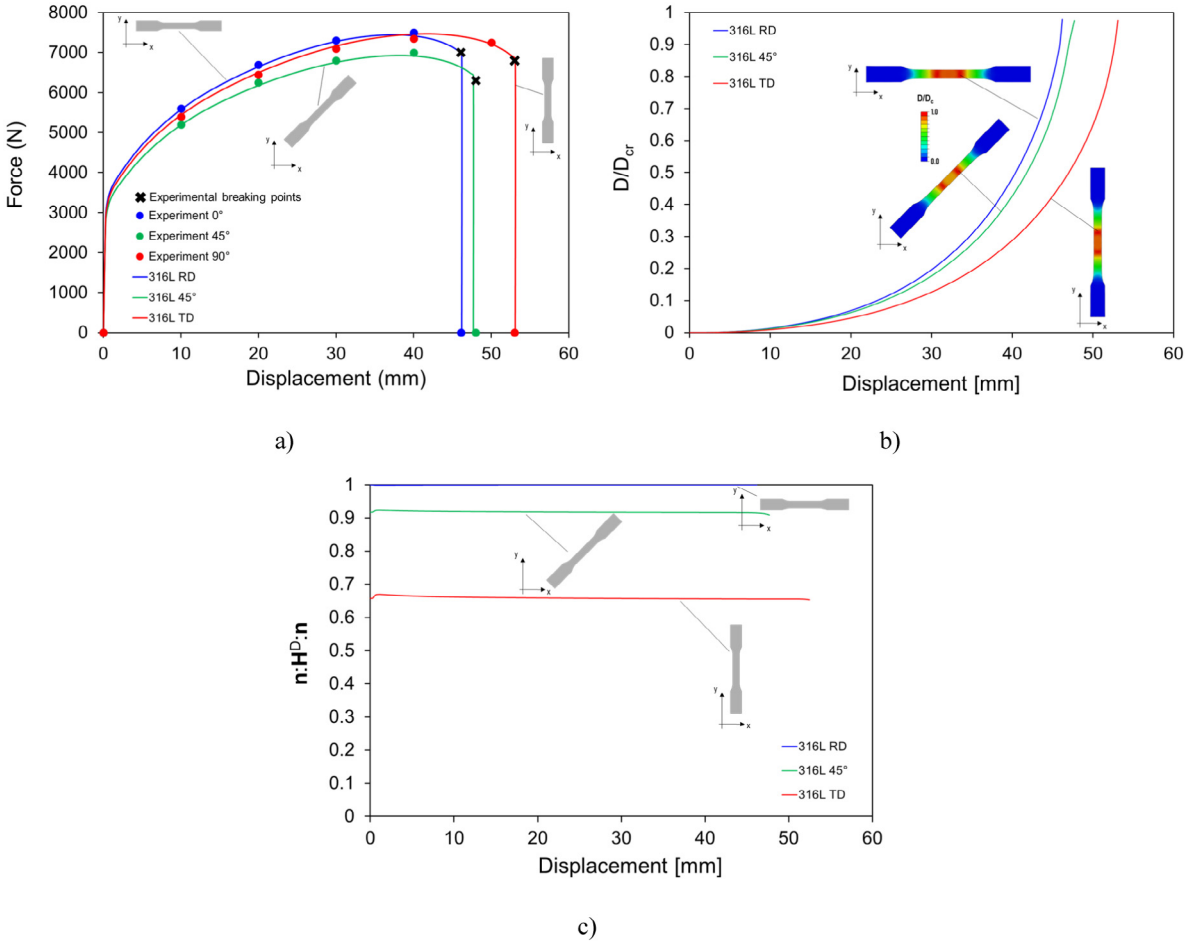

Fig. 8. (a) Force vs. displacement curves for the three samples where the black markers indicate the experimental breaking points, (b) Damage evolution vs. displacement for the elements with the highest damage accumulations (c) $\mathbf{n}:\mathbf{H}^D:\mathbf{n}$ multiplier for the three samples. (For interpretation of the references to colour in this figure legend, the reader is referred to the web version of this article.)

of 0.65 throughout the analysis, and it determines a damage accumulation 35% lower along TD compared to the RD direction. This choice of F^D was validated for the sample 45° as reported using a green solid line in Fig. 8a. The force– displacement curve is well described by the model as well as the final displacement to failure. A slight overestimation of the damage accumulation is predicted. The damage evolution for the elements with the highest damage accumulation is reported in Fig. 8c for the three specimens. The different accumulation of the damage is a direct consequence of the values assumed by the multiplier $\mathbf{n}:\mathbf{H}^D:\mathbf{n}$.

An additional test was conducted to verify the frame invariance of the kinematic framework of the DEOSS. The numerical results for the TD sample in Fig. 8 (indicated hereafter with the label 'w/o R') were compared with the numerical data obtained by performing the same tensile test with a superposed rotation of 90° (indicated with 'w R') as schematically represented in Fig. 9a and b. The graphs in Figs. 9c and 8d display a perfect match of the global (force vs. displacement curves) and local (damage and $\mathbf{n}:\mathbf{H}^D:\mathbf{n}$ evolutions) results, proving the correct implementation of the algorithm.

3.5. Carbon steel notched round bars and flat grooved plates

This last numerical test deals with the failure behaviour of low-carbon construction steel. The experimental characterisation and the numerical simulations of three notched round bars and four flat grooved plates were

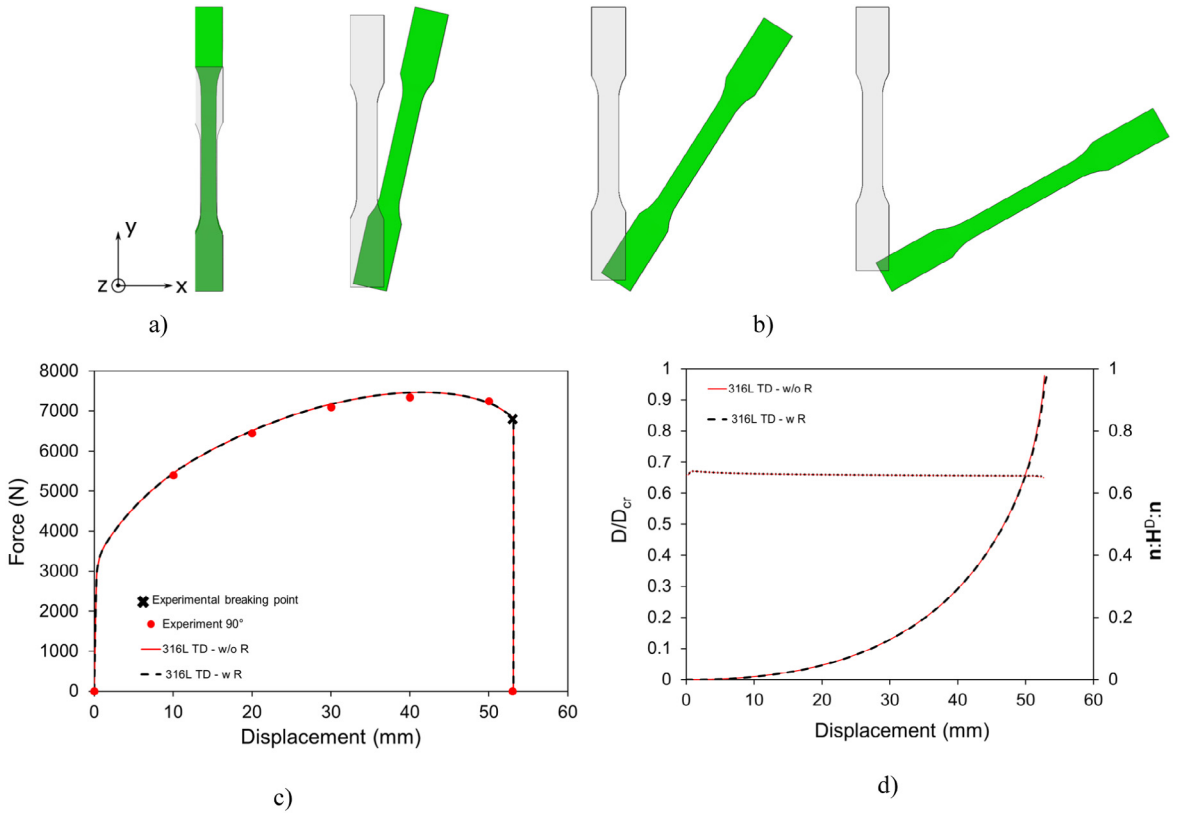

Fig. 9. (a) Sketch of the TD tensile test without rotation 'w/o R' (b) Sketch of the TD tensile test with rotation 'w R' (c) Force vs. displacement curves, (d) Damage and damage multiplier evolution vs. displacement.

conducted in a previous work of the authors Tsutsumi et al. [19]. In particular, the previous work adopted a partially coupled elasto-plastic and damage model developed by Fincato and Tsutsumi [25] with a Mohr–Coulomb failure criterion [16]. The present paper aims to reproduce the experimental results using the DEOSS model.

The details of the experiments and additional information on the geometry and modelling of the specimens can be found in the study by Tsutsumi et al. [19] (see Fig. 10). Briefly, the notched round bars have notch radii of 2, 8.75 and 17.5 mm, respectively. The same dimension of the grooves was used for the flat plates with the addition of a fourth sample with a groove radius of 35 mm. All the analyses considered monotonic tensile loading conditions up to failure and accounted for quasi-static loading conditions. Since the material did not show a relevant anisotropic behaviour, the parameters for the Hill48 criterion were set to unity, recovering a von Mises plastic potential. Similarly, the coefficients for the $\mathbf{H}^D$ were also assumed to be unitary with the exception of the b1 constant, which is relevant for the diversification of the damage evolution under plane strain conditions (i.e. $\overline{\theta} = 0$). Table 13 reports the viscoplastic and damage constants of the DEOSS model used in the simulations. Since the analyses are limited to monotonic tensile tests the constant c_s was set to 0, neglecting the effect of the similarity centre. In particular, the choice of the s_1 and s_2 parameters was assumed to cause a sudden material failure in the proximity of the final elongation to failure. This assumption was made due to further investigation of the low-carbon construction steel, which pointed out the low presence of impurities and no void formation even under large plastic deformations. Therefore, the mechanism of void formation, growth and coalescence was assumed to rapidly progress towards the end of the tensile tests. The values assigned to s_1 and to the exponent s_2 are able to phenomenologically describe the phenomenon.

Figs. 11a and 10b report the axial stress and damage evolution vs. the axial strain for the notched bars and round plates. The dashed curves indicate the experimental data where the breaking points of the specimens are marked with a hollow 'x'; the solid lines were obtained using the DEOSS model. The failure in the numerical

Table 13
Viscoplastic and damage material constants for the 316L steel.

Elastic modulus	206 [GPa]
υ	0.3
h_1, h_2	0.17, 6.5
R_e	0.3
C_1, B_1	2000 [MPa], 9
C_2, B_2	190 [MPa], 0.1
u	10 000
F_0	340 [MPa]
s_1, s_2	365 [MPa], 7.0
b_1	2.0
D_c	0.2

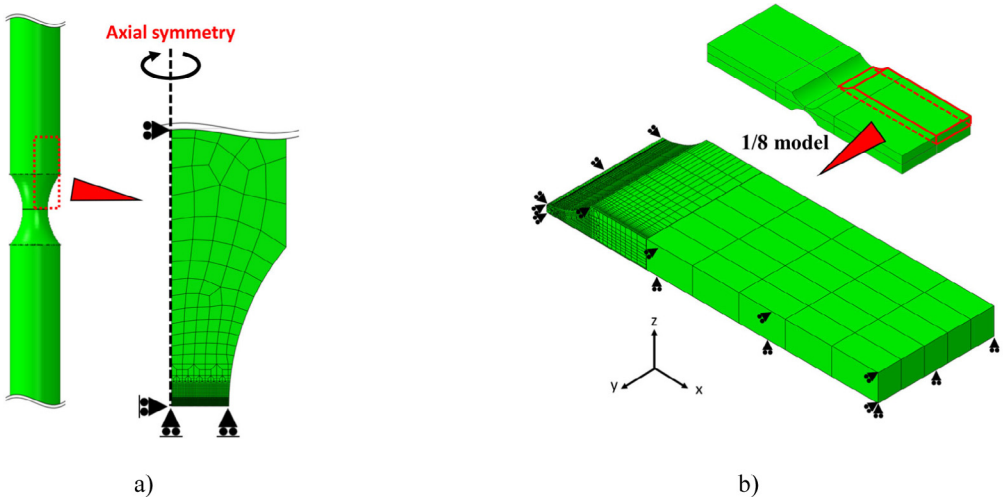

Fig. 10. (a) Schematic representation of the boundary conditions and geometry adopted for (a) notched bars and (b) flat grooved plates as in Fig. 5 in the study by Tsutsumi et al. [19].

simulation is indicated with a coloured 'x' marker. The numerical results seem to be in good agreement with the experiments. A slight underestimation of the axial stress is observed with the exception of the flat grooved plate R2.0. Better calibration of the hardening parameters could help overcome this drawback. Moreover, the final deformation to fracture is well described with small discrepancies between the experiments and the simulations. The only exception is presented by the flat plate with an 8.75 mm groove where the model seems to overestimate the material performance. Overall, the results can be considered acceptable.

Figs. 11c and 10d show the evolution of the stress triaxiality, the Lode angle parameter and the damage multiplier $\mathbf{n} : \mathbf{H}^D : \mathbf{n}$ against the cumulative plastic strain. The two graphs report the variable for the elements with the highest damage accumulation. First, the DEOSS results are consistent with the numerical results reported by Tsutsumi et al. [19], displaying the same location for crack formation (see Fig. 12) and the same trends for stress triaxiality evolution. Second, the role of the parameter b_1 can be evaluated by observing Fig. 11b and d. The lode angle parameter for the flat plates assumes a unitary value at the beginning of the loading; however, it rapidly decreased to 0 around 0.25% axial strain. As a consequence of this aspect, the damage multiplier $\mathbf{n} : \mathbf{H}^D : \mathbf{n}$ also assumes an initial unitary value, and it increases to the value of b_1 when the plane strain condition is achieved, giving an acceleration to the damage evolution. The results are visible in Fig. 11b where the damage evolution is reported by considering $b_1 = 1$ and $b_1 = 2$. In the first case, the ductile damage evolution law is identical to the original Lemaitre's formulation and overestimates the final axial deformation to fracture (i.e. dotted lines). On the contrary, in the second case, the Lode angle effect can be accounted for, and a more realistic failure description for the plates is obtained.

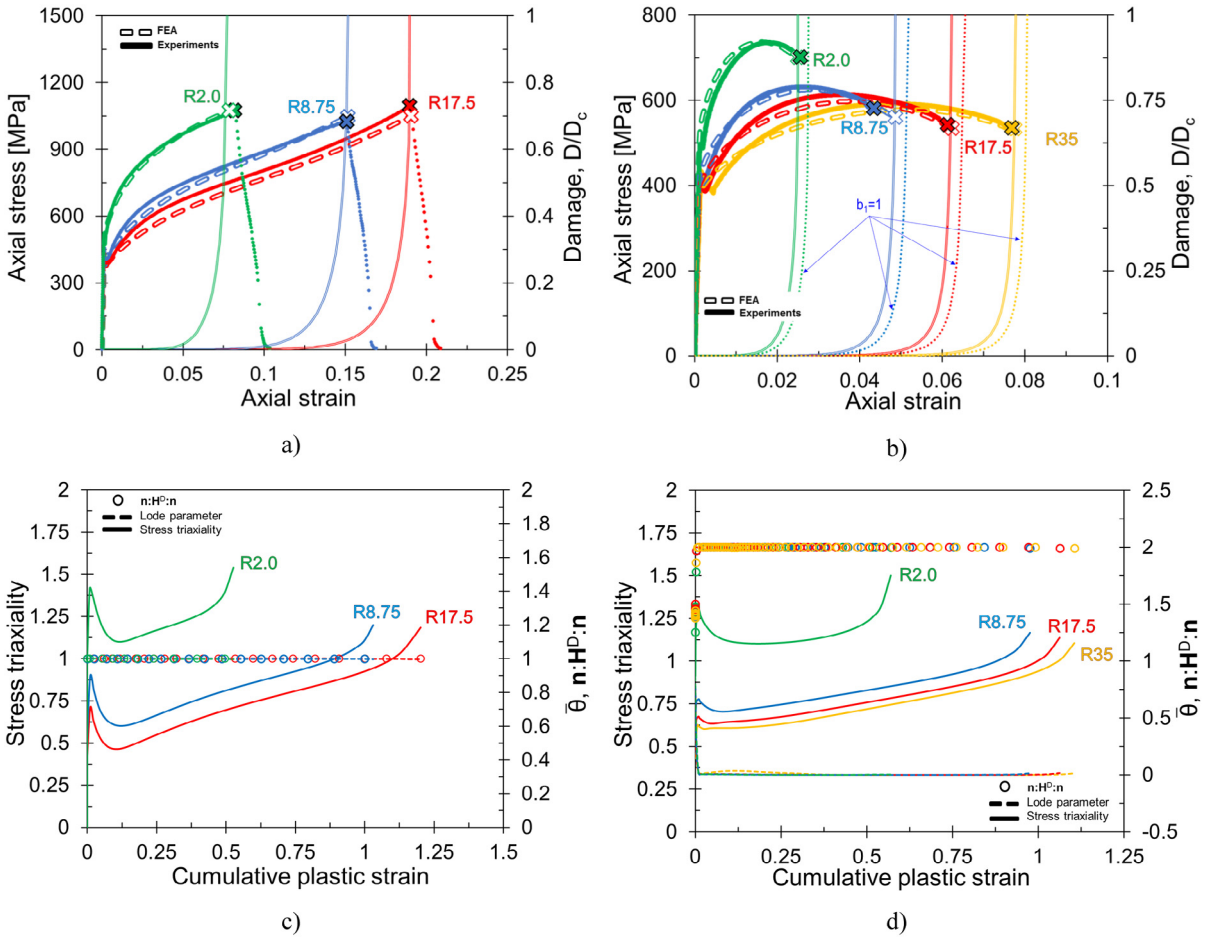

Fig. 11. Axial stress vs. axial strain (a) for the notched round bars, (b) flat grooved plates. Stress triaxiality, Lode angle parameter and damage multiplier $\mathbf{n}:\mathbf{H}^{D}:\mathbf{n}$ against the cumulative plastic strain (c) for the notched round bars, (d) for the flat grooved plates.

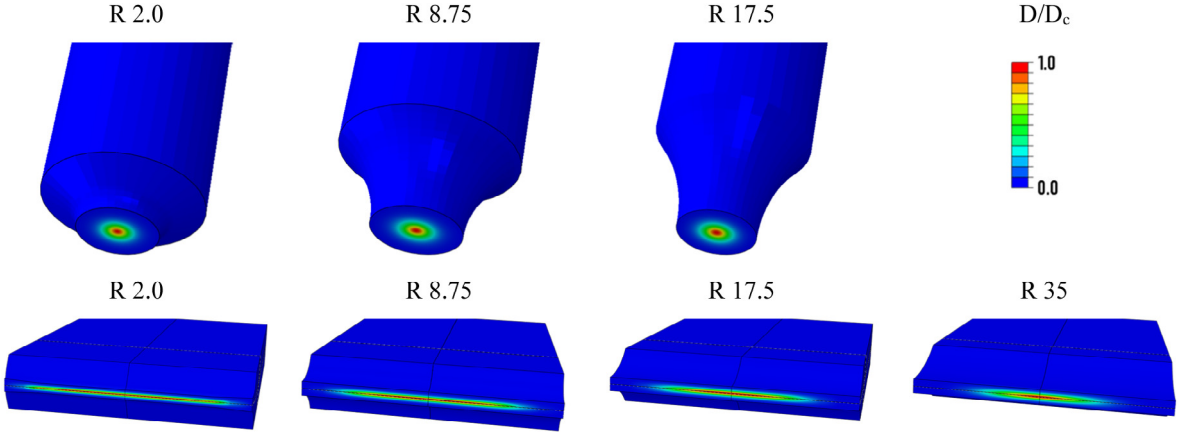

Fig. 12. Damage contour field at failure for the round notched bars and flat grooved plates.

4. Limitation of the present formulation of the DEOSS model

The current formulation presents certain limitations. In this section, some of the aspects that need further improvements or that have been neglected are considered.

- The novel damage law defined in Eq. (16) offers quite a simple criterion to judge the damage evolution, thereby allowing one to enhance the damage rate depending on the stress state and the loading conditions. The additional term, introduced by the tensors $\mathbf{n}$ and $\mathbf{H}^{\mathrm{D}}$, returns a scalar multiplier that cannot consider the full complexity of an anisotropic damage variable. It can simply be representative of the tendency of the damage to accumulate faster (or slower) along certain directions than others. Moreover, it requires the calibration of seven constants, which, however, can be obtained with simple tensile and shear tests.
- The model has been developed within the framework of *phenomenological* damage models [35] following the approach initially proposed by [119] and Lemaitre [24,60]. The approach does not consider plastic volume variation since the coupled yield criterion is a function of the deviatoric part of the stress [2]. Hammi and Horstemeyer [120] proposed a phenomenological model with a damage evolution law accounting for nucleation, growth and coalescence. Micro-mechanical based models [30,31,33,42,50] can give a better description of the void nucleation, growth and coalescence process however they are characterised by other drawbacks [2,14,35].
- As the damage progresses, the material decreases its load-bearing capacity and becomes prone to strain and damage localisations. This pathological mesh dependency is not related to the FEM itself, but it occurs due to the definition of the constitutive behaviour of the material. In the present work, the localisation of the damage and the plastic strain was avoided by the definition of a critical damage value that was much lower than unity ($\sim 0.2 \div 0.25$). Whenever the damage reaches the value of D_c the crack can be considered as formed, allowing one to avoid an excessive loss of stiffness and the related loss of quadratic rate of convergence in the return mapping scheme as pointed out by de Souza Neto et al. [15]. However, to overcome this drawback, alternative and better strategies can be adopted. In general, two main approaches have been developed: the addition of a 'spatial averaging term' in terms of a characteristic length in the material formulation (e.g. Andrade et al. [121]; Marotti de Sciarra, [122,123]) or the adoption of a gradient-like definition of the internal variables such as the plastic strain and the damage [124–128]. Both approaches result in mesh-independent solutions, but the implementation of gradient-type formulations seems to be more straightforward, especially in terms of adopting user-defined subroutines for commercial codes. Future works will aim to analyse this aspect.
- The set of analyses presented in Section 3 dealt with relatively simple loading conditions where the load was applied proportionally. In a previous work [63], the authors investigated the effect of the non-proportionality of the loading condition on the damage evolution by means of the tangential plasticity contribution. In the present formulation, this aspect was not considered. Nevertheless, the adoption of an anisotropic yield function in combination with a damage evolution law that considers the directionality of the load might be able to simulate the material failure under non-proportional loading. This aspect will be verified in future works.
- Except for the cyclic loading analysis on the lead-free solder material, all the numerical simulations reproducing experimental data were carried out within a relatively small range of stress triaxialities ($1/3 \leq \eta$). Proper verification of the DEOSS model's ability to describe the material failure should be conducted by investigating a wider range of loading conditions and the geometries of different samples as in some previous works [22,129,130].
- The present work does not consider the micro-cracks closure effect (Andrade Pires et al. [131]; Badreddine and Saanouni, [48]; Kumar and Dixit, [132]; Yue et al. [133]; Zhang et al. [22]; among others) that was observed for loading paths' alternating tension and compression phases. This additional aspect must be taken into consideration for future works on low cycle fatigue or for loading paths while considering compression.
- Several experimental works (e.g., Benaarbia et al. [134]; Oppermann et al. [135]; Roy Chowdhury et al. [136, 137]; among others) pointed out that temperature plays a fundamental role in the mechanical response of metallic materials. The inclusion of the temperature as an internal variable in the constitutive equations of the DEOSS model represents a future challenge.

5. Conclusions

The paper extends the work of the authors carried out in a previous study (i.e. the EOSS model in the study by Fincato and Tsutsumi, [57]) and enriches the set of constitutive equations to describe the ductile damage behaviour of pressure insensitive metallic materials within the framework of the CDM. Moreover, a few other aspects of the EOSS model are improved. The current formulation can account for plastic anisotropy with the inclusion of the Hill48 yield criterion together with a different computational kinematic framework based on the kinetic logarithmic spin, thereby eliminating several drawbacks connected with the use of the Jaumann co-rotational spin.

A novel scalar damage evolution law is proposed as a simple and practical criterion to describe the material failure under several loading conditions. By means of simple tensile tests, it is possible to calibrate the material parameters affecting the damage variable to consider a damage evolution that depends on the loading directions in relation to the axes of anisotropy. Moreover, it was found that the model is able to catch a different deformation to fracture observed under plane strain conditions. Several numerical examples were provided to explain the role of the material parameters in the novel damage evolution law. Several experimental data were reproduced using the DEOSS model and dealing with cyclic loading on a lead-free solder material with the tensile tests on a 316L steel and the tensile tests on low-carbon construction steel notched round bars and flat grooved plates resulting in an acceptable description of the mechanical behaviours in all the tests.

The limitations of the current formulation of the theory were discussed along with the possible strategies and solutions adopted by several authors in the literature. Future works will develop the DEOSS model further to eliminate the aforementioned shortcomings.

Nomenclature

$\mathbb{C}^{TO}$: consistent tangent operator;
$\mathbf{E}^0$: fourth-order elasticity tensor (undamaged conf.);
$\mathbf{E}$: fourth-order elasticity tensor (damaged conf.);
$\mathbf{H}$: *Hill48* yield criterion tensor;
$\mathbf{H}^{\mathrm{D}}$: damage Hill-like tensor;
$\mathbf{D}$, $\boldsymbol{\varepsilon}$: strain rate tensor, strain tensor;
$\mathbf{D}^{\mathrm{e}}$, $\boldsymbol{\varepsilon}^{\mathrm{e}}$: elastic strain rate tensor, elastic strain tensor;
$\mathbf{D}^{\mathrm{vp}}$, $\boldsymbol{\varepsilon}^{\mathrm{vp}}$: viscoplastic strain rate tensor, viscoplastic strain tensor;
$\mathbf{D}^{vp}_{ss}$, $\boldsymbol{\varepsilon}^{vp}_{ss}$, similarity centre storage viscoplastic strain rate tensor and viscoplastic strain tensor;
$\mathbf{D}^{vp}_{sd}$, $\boldsymbol{\varepsilon}^{vp}_{sd}$, similarity centre dissipative viscoplastic strain rate tensor and viscoplastic strain tensor;
$\mathbf{D}^{vp}_{ks}$, $\boldsymbol{\varepsilon}^{vp}_{ks}$, back stress storage viscoplastic strain rate tensor and viscoplastic strain tensor;
$\mathbf{D}^{vp}_{kd}$, $\boldsymbol{\varepsilon}^{vp}_{kd}$, back stress dissipative viscoplastic strain rate tensor and viscoplastic strain tensor;
$\mathbf{W}$: continuum spin tensor;
$\mathbf{W}^{\mathrm{p}}$: plastic spin tensor;
$\boldsymbol{\Omega}^{k\log}$: kinetic logarithmic spin;
$\mathbf{B}^k$: left Cauchy–Green deformation tensor;
$\Delta\boldsymbol{\Lambda}$, $\delta\boldsymbol{\Lambda}$: incremental rotation tensors from the current to the rotation-insensitive configuration;
$\mathbf{L}$: velocity gradient;
$\boldsymbol{\tau}$: Kirchhoff stress tensor;
$\boldsymbol{\sigma}$: Cauchy stress tensor;
$\boldsymbol{\sigma}_y$: Cauchy stress tensor on the normal-yield surface;
$\boldsymbol{\sigma}_{ss}$: Cauchy stress tensor on the subloading surface;
$\boldsymbol{\alpha}$: back stress tensor;
$\mathring{\boldsymbol{\sigma}}$: co-rotational rate of the Cauchy stress;
$\mathring{\boldsymbol{\alpha}}$: co-rotational rate of the back stress;
$\overline{\boldsymbol{\sigma}}$: conjugate Cauchy stress for the dynamic loading surface;
$\overline{\boldsymbol{\sigma}}_{ss}$: conjugate Cauchy stress for the subloading surface;
$\overline{\boldsymbol{\alpha}}$: conjugate back stress for the dynamic loading surface;
$\overline{\boldsymbol{\alpha}}_{ss}$: conjugate back stress for the subloading surface;
$\widetilde{\boldsymbol{\sigma}}$: Cauchy stress observed from the similarity-centre;

$\boldsymbol{s}$: similarity centre tensor;
$\hat{\mathbf{s}}$: similarity-centre observed from the back stress;
$\overline{\mathbf{N}}$: normalised outward normal tensor to the plastic potential;
G: shear modulus;
υ: Poisson's ratio;
F: isotropic hardening function;
F_0: initial size of normal-yield surface (i.e., yield stress);
H: cumulative plastic strain variable;
R: subloading surface similarity ratio;
R_d: dynamic loading surface similarity ratio;
R_e: constant defining the size of the elastic subdomain;
R_m: constant limiting the maximum size of the dynamic loading surface;
α: plastic spin anisotropic constant;
λ: viscoplastic multiplier;
μ: viscoplastic coefficient;
n: rate-sensitivity material constant;
C_i, B_i: material constants for the kinematic hardening;
s_1, s_2: damage coefficients;
Y: damage energy release rate;
F, G, H, L, M, N: *Hill48* anisotropic coefficients;
F^D, G^D, H^D, L^D, M^D, N^D, b_1: damage anisotropic coefficients;
ψ: total Helmholtz free energy;
ψ_{ed}: free energy associated with the elasticity;
ψ_{pk}: free energy associated with the back stress;
ψ_{ps}: free energy associated with the similarity centre;
ψ_{pi}: free energy associated with the isotropic hardening;
ϕ_d : total mechanical dissipation;
ϕ_{dp} : viscoplastic dissipation;
ϕ_{dd} : damage dissipation;
f: generic stress function expressing the plastic potential;
h_1, h_2: material parameters for the isotropic hardening;
u: material constant for the similarity ratio evolution;
χ: parameter limiting movement of $\boldsymbol{s}$;
c_s: constant influencing $\boldsymbol{s}$ translation speed;
η: stress triaxiality;
$\overline{\theta}$: Lode angle parameter.
EOSS: Extended overstress subloading surface model (rate-dependent);
DEOSS: Damage extended overstress subloading surface model (rate-dependent);

Declaration of competing interest

The authors declare that they have no known competing financial interests or personal relationships that could have appeared to influence the work reported in this paper.

Appendix

The constitutive equations of the DEOSS model require the use of an incrementally objective integration algorithm to maintain the frame invariance with respect to rigid body motions. This incrementally objective integration algorithm is well established and has been adopted in several commercial and non-commercial FE codes; details can be found in the studies by de Souza Neto et al. [15], Hughes and Winget [138] and Simo and Huges [71], among others. The idea is to solve the system of constitutive equations formulated in the current configuration in a configuration unaffected by any superposed spatial rigid body motion. Only the main aspects of the integration algorithm are discussed here; a step-by-step and exhaustive description of the incrementally objective update formula

for hypoelastic-based plasticity models can be found in the studies by Brepols et al. [66], Jiao and Fish [61] and Palizi et al. [139].

Considering the body in equilibrium at a generic time $t_n \subset [0, t]$, the purpose is the computation of the set of unknowns $\mathbf{x}_{n+1} = \left[\boldsymbol{\sigma}_{n+1}, R_{d,n+1}, H_{n+1}, R_{n+1}, D_{n+1}, \mathbf{s}_{n+1}, \boldsymbol{\alpha}_{n+1}\right]$ defining the new mechanical equilibrium at the subsequent time $t_{n+1} = t_n + \Delta t$ with $t_{n+1} \subset [0, t]$. The formulation of all the variables in this rotation-neutralised configuration passes through the definition of two orthogonal rotation tensors $\Delta\boldsymbol{\Lambda}$ and $\delta\boldsymbol{\Lambda}$ obtained by means of the skew-symmetric spin tensor $\boldsymbol{\Omega}^{k\log}$ as follows:

$$\Delta\boldsymbol{\Lambda} \approx \exp\left(\int_{t_n}^{t_{n+1}} \boldsymbol{\Omega}^{k\log} dt\right); \qquad \delta\boldsymbol{\Lambda} \approx \exp\left(\frac{1}{2}\int_{t_n}^{t_{n+1}} \boldsymbol{\Omega}^{k\log} dt\right) \tag{20}$$

The tensors $\Delta\boldsymbol{\Lambda}$ and $\delta\boldsymbol{\Lambda}$ are incremental rotations from the n to the $n + 1$ configuration and from the $n + 1/2$ to the $n + 1$ configuration that can be used to rotate the variables in the current configuration to obtain an updated formula of the unknowns that is rigid-motion-insensitive.

The resolution strategy adopts a multi-equation Newton–Raphson scheme, which is also known as the return mapping method, in the form discussed in previous works of the authors [57,64,140]. At the beginning of the computation, the trial elastic is performed to evaluate the stress state at the time t_{n+1} (i.e. $\boldsymbol{\sigma}_{n+1}$), thereby providing the increment of strain $\Delta\boldsymbol{\varepsilon} = \Delta t\, \mathbf{D}$ and 'freezing' all the plastic and damage internal variables. If the new stress state represents an admissible state for the material, then the equilibrium at t_{n+1} is fulfilled; otherwise, a viscoplastic correction is performed through a series of k sub-iterations until the fulfilment of the equilibrium. Hereafter, the viscoplastic correction procedure is briefly explained.

In the context of FE codes with reference to the Abaqus UMAT user subroutine, the integration is performed on the Gauss points at a local level. Different input and output need to be provided for the computational step at the time t_{n+1}:

- INPUT: the set of unknowns and the information about the orientation of the axes of anisotropy at the previous equilibrium point $\mathbf{x}_n = \left[\boldsymbol{\sigma}_n, R_{d,n}, H_n, R_n, D_n, \mathbf{s}_n, \boldsymbol{\alpha}_n\right]$; $\mathbf{H}_n$ and $\mathbf{H}_n^D$; the two deformation gradients $\mathbf{F}_{n+1}$ and $\mathbf{F}_{n+1}$; the time interval Δt and the relevant state variables.
- OUTPUT: an updated set of unknowns $\mathbf{x}_{n+1}$; the updated information about the orientation of the axes of anisotropy $\mathbf{H}_{n+1}$ and $\mathbf{H}_{n+1}^D$; the consistent tangent operator $\mathbb{C}^{TO}$ for the convergence of the global mechanical equilibrium and the updated state variables.

First, an approximation of the two rotation tensors in Eq. (20) can be rewritten as in Eq. (21) where the contribution of the plastic spin is neglected since an elastic trial is assumed, but $\mathbf{W}^{\mathrm{p}}$ needs to be considered in the viscoplastic correction algorithm:

$$\begin{aligned} \Delta\Lambda^{(k)} &\approx \exp\left[\Delta t\mathbf{W}_n + \overline{\mathbf{W}}_n^{k\log}\left(\mathbf{B}^k\left(\boldsymbol{\sigma}_n, D_n\right), \Delta t\mathbf{D}_n\right)\right] \\ \delta\Lambda^{(k)} &\approx \exp\left[\frac{1}{2}\left(\Delta t\mathbf{W}_n + \overline{\mathbf{W}}_n^{k\log}\left(\mathbf{B}^k\left(\boldsymbol{\sigma}_n, D_n\right), \Delta t\mathbf{D}_n\right)\right)\right]. \end{aligned} \tag{21}$$

where $\mathbf{W}$ and $\mathbf{D}$ are the same terms introduced in Eq. (1) and are re-written here as follows:

$$\begin{aligned} \mathbf{D}_n &\approx \frac{1}{2\Delta t}\mathbf{F}_n^{-T}\left(\mathbf{F}_{n+1}^T\mathbf{F}_{n+1} - \mathbf{F}_n^T\mathbf{F}_n\right)\mathbf{F}_n^{-1} \\ \mathbf{W}_n &\approx \frac{1}{2\Delta t}\left(\mathbf{F}_{n+1}\mathbf{F}_n^{-1} - \mathbf{F}_n^{-T}\mathbf{F}_{n+1}^T\right) \end{aligned} \tag{22}$$

The trial elastic was performed as follows:

$$
\begin{aligned}
&D_{n+1}^{(k)} = D_n \\
&\boldsymbol{\sigma}_{n+1}^{(k)} = \Delta\Lambda^{(k)}\boldsymbol{\sigma}_n\Delta\Lambda^{T,(k)} + \left(1 - D_{n+1}^{(k)}\right)\mathbf{E}^0 \colon \left[\delta\Lambda^{(k)}\left(\Delta t\,\mathbf{D}_{n+1/2}\right)\delta\Lambda^{T,(k)}\right] \\
&\boldsymbol{\alpha}_{n+1}^{(k)} = \Delta\Lambda^{(k)}\boldsymbol{\alpha}_n\Delta\Lambda^{T,(k)} \\
&\mathbf{s}_{n+1}^{(k)} = \Delta\Lambda^{(k)}\mathbf{s}_n\Delta\Lambda^{T,(k)} \\
&\mathbf{H}_{n+1}^{(k)} = \Delta\Lambda^{(k)}\Delta\Lambda^{(k)}\mathbf{H}_n\Delta\Lambda^{T,(k)}\Delta\Lambda^{T,(k)} \\
&\mathbf{H}_{n+1}^{D,(k)} = \Delta\Lambda^{(k)}\Delta\Lambda^{(k)}\mathbf{H}_n^{D}\Delta\Lambda^{T,(k)}\Delta\Lambda^{T,(k)} \\
&H_{n+1}^{(k)} = H_n; \quad R_{n+1}^{(k)} = R_n; \quad R_{d,n+1}^{(k)} = R_{d,n}
\end{aligned}
\tag{23}
$$

where the isotropy of the elasticity tensor is exploited and the term $\Delta t\,\mathbf{D}_{n+1/2}$ can be obtained from the deformation gradients $\Delta t\,\mathbf{D}_{n+1/2} = 1/2\mathbf{F}_{n+1/2}^{-T}\left(\mathbf{F}_{n+1}^{T}\mathbf{F}_{n+1} - \mathbf{F}_n^{T}\mathbf{F}_n\right)\mathbf{F}_{n+1/2}^{-1}$. In case viscoplastic correction is needed, the procedure the set of equations reported in Box 1 (Section 2.2) can be written as follows:

$$
\mathbf{b}_{n+1}^{(k)} = \begin{bmatrix}
\sqrt{3/2}\left|\overline{\boldsymbol{\sigma}}_{n+1}^{(k)} \colon \mathbf{H}_{n+1}^{(k)} \colon \overline{\boldsymbol{\sigma}}_{n+1}^{(k)}\right| - \left(1 - D_{n+1}^{(k)}\right) R_{d,n+1}^{(k)} \underset{\sim}{F}\left(H_{n+1}^{(k)}\right) \\
\boldsymbol{\sigma}_{n+1}^{(k)} - \dfrac{\left(1 - D_{n+1}^{(k)}\right)}{(1 - D_n)}\Delta\Lambda^{(k)}\boldsymbol{\sigma}_n\Delta\Lambda^{T,(k)} + \left(1 - D_{n+1}^{(k)}\right)\mathbf{E}^0 \colon \left[\delta\Lambda^{(k)}\left(\Delta t\,\mathbf{D}_{n+1/2}\right)\delta\Lambda^{T,(k)}\right] \\
\qquad + \dfrac{1}{\mu}\dfrac{\left\langle \exp\left(n\left[R_{d,n+1}^{(k)} - R_{n+1}^{(k)}\right]\right) - 1\right\rangle}{\left(R_m - R_{d,n+1}^{(k)}\right)} 2G\mathbf{N}_{n+1}^{(k)}\Delta t \\
\mathbf{s}_{n+1}^{(k)} - \dfrac{\left(1 - D_{n+1}^{(k)}\right)}{(1 - D_n)}\Delta\Lambda^{(k)}\mathbf{s}_n\Delta\Lambda^{T,(k)} - \mathring{\mathbf{s}}_{n+1}^{(k)}\Delta t \\
H_{n+1}^{(k)} - H_n - \sqrt{\dfrac{2}{3}}\dfrac{1}{\mu}\dfrac{\left\langle \exp\left(n\left[R_{d,n+1}^{(k)} - R_{n+1}^{(k)}\right]\right) - 1\right\rangle}{\left(1 - D_{n+1}^{(k)}\right)\left(R_m - R_{d,n+1}^{(k)}\right)}\Delta t \\
R_{n+1}^{(k)} - R_e - \dfrac{2}{\pi}(1 - R_e)\cos^{-1}\left[\cos\left(\dfrac{\pi}{2}\dfrac{R_0 - R_e}{1 - R_e}\right)\exp\left(-u\dfrac{\pi}{2}\dfrac{\mathbf{D}_{n+1}^{vp}\Delta t}{1 - R_e}\right)\right] \\
D_{n+1}^{(k)} - D_n - \sqrt{\dfrac{2}{3}}\dfrac{\lambda}{\left(1 - D_{n+1}^{(k)}\right)}\left(-\dfrac{Y_{n+1}^{(k)}}{s_1}\right)^{s_2}\mathbf{n}_{n+1}^{(k)} \colon \mathbf{H}_{n+1}^{D,(k)} \colon \mathbf{n}_{n+1}^{(k)} \\
\boldsymbol{\alpha}_{n+1} - \dfrac{\left(1 - D_{n+1}^{(k)}\right)}{(1 - D_n)}\Delta\Lambda^{(k)}\boldsymbol{\alpha}_n\Delta\Lambda^{T,(k)} - \mathring{\boldsymbol{\alpha}}_{n+1}^{(k)}\Delta t
\end{bmatrix}
\tag{24}
$$

The co-rotational rates of the back stress and the similarity centre are not rotated by $\delta\boldsymbol{\Lambda}$ as well as the viscoplastic correction term in the equation of the stress; therefore, an approximation used in the study by Jiao and Fish (2018) is adopted. The updated set of unknowns is computed as follows:

$$
\mathbf{x}_{n+1}^{(k+1)} = \mathbf{x}_{n+1}^{(k)} - \left[\mathbf{A}_{n+1}^{(k)}\right]^{-1}\mathbf{b}_{n+1}^{(k)} = \mathbf{x}_{n+1}^{(k)} - \delta\mathbf{x}_{n+1}^{(k+1)}
\tag{25}
$$

where $\mathbf{A}$ represents the matrix of the partial derivatives, i.e. the Jacobian matrix, which is obtained by deriving the set of equations in Eq. (24) against the unknowns. It should be pointed out that the definition of the tensors $\Delta\boldsymbol{\Lambda}$ and $\delta\boldsymbol{\Lambda}$ depends on the damage as well as on the plastic strain. Once updated, the unknowns, all the variables (e.g. $F_{n+1}^{(k+1)}$, $\overline{\mathbf{N}}_{n+1}^{(k+1)}$, $\mathbf{n}_{n+1}^{(k+1)}\ldots$) to the $k+1$ sub-iteration and the tensors $\Delta\boldsymbol{\Lambda}$ and $\delta\boldsymbol{\Lambda}$ are evaluated again, and the

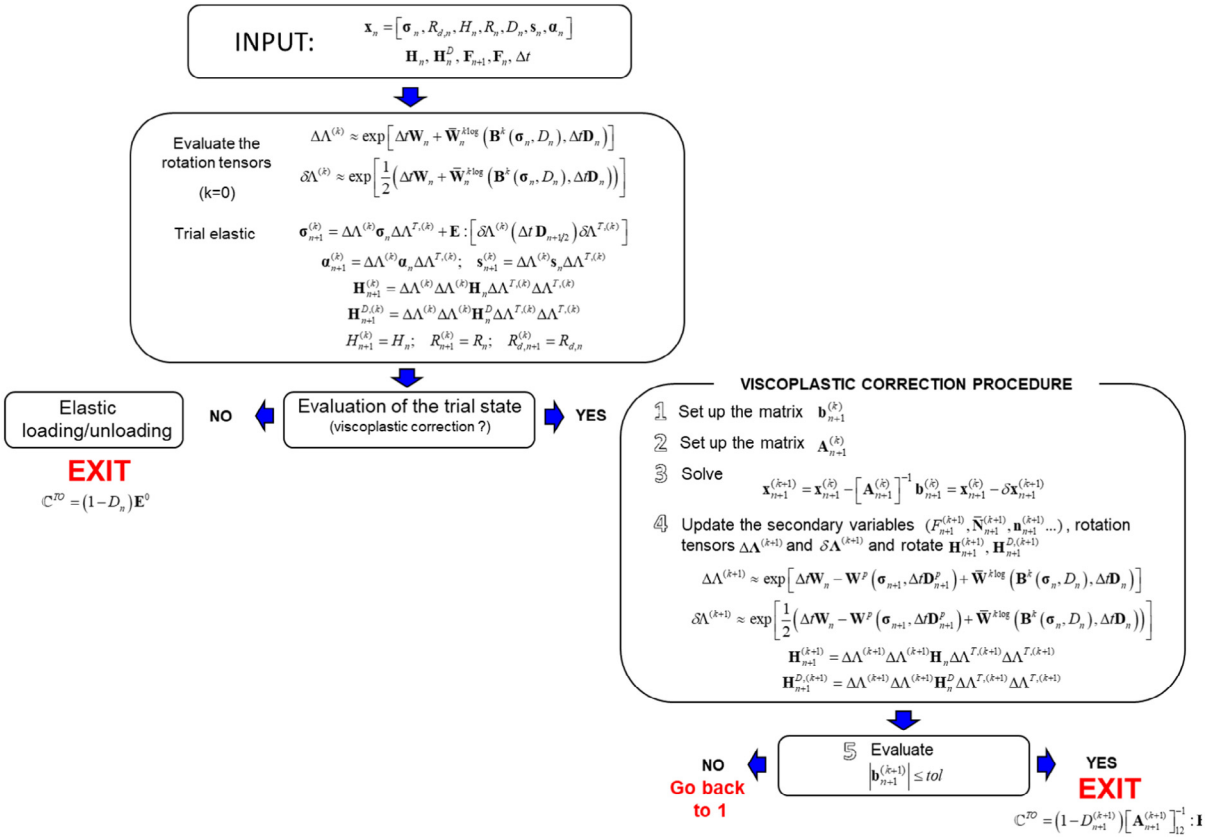

Fig. 13. Flow chart of the DEOSS model for the user subroutine UMAT (Abaqus).

rotation of the $\mathbf{H}_n$ and $\mathbf{H}_n^D$ tensors is performed:

$$\begin{aligned}
\Delta\Lambda^{(k+1)} &\approx \exp\left[\Delta t\mathbf{W}_n - \mathbf{W}^p\left(\boldsymbol{\sigma}_{n+1}, \Delta t\mathbf{D}^p_{n+1}\right) + \overline{\mathbf{W}}^{k\log}\left(\mathbf{B}^k\left(\boldsymbol{\sigma}_n, D_n\right), \Delta t\mathbf{D}_n\right)\right] \\
\delta\Lambda^{(k+1)} &\approx \exp\left[\frac{1}{2}\left(\Delta t\mathbf{W}_n - \mathbf{W}^p\left(\boldsymbol{\sigma}_{n+1}, \Delta t\mathbf{D}^p_{n+1}\right) + \overline{\mathbf{W}}^{k\log}\left(\mathbf{B}^k\left(\boldsymbol{\sigma}_n, D_n\right), \Delta t\mathbf{D}_n\right)\right)\right] \\
\mathbf{H}^{(k+1)}_{n+1} &= \Delta\Lambda^{(k+1)}\Delta\Lambda^{(k+1)}\mathbf{H}_n\Delta\Lambda^{T,(k+1)}\Delta\Lambda^{T,(k+1)} \\
\mathbf{H}^{D,(k+1)}_{n+1} &= \Delta\Lambda^{(k+1)}\Delta\Lambda^{(k+1)}\mathbf{H}^D_n\Delta\Lambda^{T,(k+1)}\Delta\Lambda^{T,(k+1)}
\end{aligned} \tag{26}$$

The viscoplastic correction stops whenever the following condition is fulfilled:

$$\left|\mathbf{b}^{(k+1)}_{n+1}\right| \leq tol \tag{27}$$

where *tol* is a threshold imposed by the user; usually $tol \leq 1.0 \times 10^{-8}$. The local procedure is summarised in the flow chart of Fig. 13. In order to guarantee the efficiency of the algorithm from a global point of view, the consistent tangent operator needs to be defined and returned as an output from the user subroutine. In this paper, we adopt the same procedure used by Fincato and Tsutsumi [57,64,140], thereby adopting a strategy that is exhaustively explained in the study by de Souza Neto et al. [15]. Briefly, once the condition in Eq. (27) is fulfilled, the consistent tangent operator can be simply obtained by the following expression:

$$\mathbb{C}^{TO} = \left(1 - D^{(k+1)}_{n+1}\right)\left[\mathbf{A}^{(k+1)}_{n+1}\right]^{-1}_{12} : \mathbf{E}^0 = \left[\mathbf{A}^{(k+1)}_{n+1}\right]^{-1}_{12} : \mathbf{E}. \tag{28}$$

where $\left[\mathbf{A}_{n+1}^{(k+1)}\right]_{12}^{-1}$ is a matrix with the same dimensions as elastic constant matrix $\mathbf{E}$ and the first term is located in the first row and second column of $\left[\mathbf{A}_{n+1}^{(k+1)}\right]^{-1}$. Lastly, the expression of the consistent tangent modulus in Abaqus must be given in terms of the Jaumann rate of the Kirchhoff stress, therefore, Eq. (28) has to be modified following the procedure in [139].

In case the viscoplastic procedure is not needed (i.e. the trial elastic state is an admissible stress state for the material), the consistent tangent operator is a function of the damage and the elasticity tensor $\mathbb{C}^{TO} = (1 - D_n)\,\mathbf{E}^0 = \mathbf{E}$.

References

[1] G. Pantazopoulos, A short review on fracture mechanisms of mechanical components operated under industrial process conditions: Fractographic analysis and selected prevention strategies, Metals (Basel) 9 (2019) 148, http://dx.doi.org/10.3390/met9020148.

[2] J. Besson, Continuum models of ductile fracture: A review, Int. J. Damage Mech. 19 (2010) 3–52, http://dx.doi.org/10.1177/1056789509103482.

[3] R. Fincato, S. Tsutsumi, T. Sakai, K. Terada, 3D crystal plasticity analyses on the role of hard/soft inclusions in the local slip formation, Int. J. Fatigue 134 (2020) 105518, http://dx.doi.org/10.1016/j.ijfatigue.2020.105518.

[4] J. Liu, M. Huang, Z. Li, L. Zhao, Y. Zhu, Microvoid growth mechanism in FCC polycrystals and a statistical damage model, Int. J. Plast. 137 (2021) 102888, http://dx.doi.org/10.1016/j.ijplas.2020.102888.

[5] A. Tang, H. Liu, R. Chen, G. Liu, Q. Lai, Y. Zhong, L. Wang, J. Wang, Q. Lu, Y. Shen, Mesoscopic origin of damage nucleation in dual-phase steels, Int. J. Plast. 137 (2021) 102920, http://dx.doi.org/10.1016/j.ijplas.2020.102920.

[6] M. Brünig, S. Gerke, J. Tix, Micro-mechanical numerical analyses on the effect of stress state on ductile damage under dynamic loading conditions, Lat. Am. J. Solids Struct. 15 (2018) http://dx.doi.org/10.1590/1679-78254945.

[7] D. An, S. Zaefferer, Formation mechanism of dislocation patterns under low cycle fatigue of a high-manganese austenitic TRIP steel with dominating planar slip mode, Int. J. Plast. 121 (2019) 244–260, http://dx.doi.org/10.1016/j.ijplas.2019.06.009.

[8] A.A. Benzerga, Micromechanical models of ductile damage and fracture, in: Handb. Damage Mech., Springer New York, New York, NY, 2013, pp. 1–22, http://dx.doi.org/10.1007/978-1-4614-8968-9_38-1.

[9] T.W.J. de Geus, F. Maresca, R.H.J. Peerlings, M.G.D. Geers, Microscopic plasticity and damage in two-phase steels: On the competing role of crystallography and phase contrast, Mech. Mater. 101 (2016) 147–159, http://dx.doi.org/10.1016/j.mechmat.2016.07.014.

[10] T. Nguyen, D.C. Francom, D.J. Luscher, J.W. Wilkerson, Bayesian calibration of a physics-based crystal plasticity and damage model, J. Mech. Phys. Solids 149 (2021) 104284, http://dx.doi.org/10.1016/j.jmps.2020.104284.

[11] A. Siddiq, A porous crystal plasticity constitutive model for ductile deformation and failure in porous single crystals, Int. J. Damage Mech. 28 (2019) 233–248, http://dx.doi.org/10.1177/1056789518757294.

[12] N. Vajragupta, V. Uthaisangsuk, B. Schmaling, S. Münstermann, A. Hartmaier, W. Bleck, A micromechanical damage simulation of dual phase steels using XFEM, Comput. Mater. Sci. 54 (2012) 271–279, http://dx.doi.org/10.1016/j.commatsci.2011.10.035.

[13] W. Zhao, S. Yang, G. Wen, X. Ren, Fractional-order visco-plastic constitutive model for uniaxial ratcheting behaviors, Appl. Math. Mech. 40 (2019) 49–62, http://dx.doi.org/10.1007/s10483-019-2413-8.

[14] L. Malcher, F.M. Andrade Pires, J.M.A. César de Sá, An assessment of isotropic constitutive models for ductile fracture under high and low stress triaxiality, Int. J. Plast. 30–31 (2012) 81–115, http://dx.doi.org/10.1016/j.ijplas.2011.10.005.

[15] E.A. de Souza Neto, D. Peric, D.R.J. Owen, Computational Methods for Plasticity, 2008, http://dx.doi.org/10.1002/9780470694626.

[16] Y. Bai, T. Wierzbicki, Application of extended Mohr–Coulomb criterion to ductile fracture, Int. J. Fract. 161 (2010) 1–20, http://dx.doi.org/10.1007/s10704-009-9422-8.

[17] M.G. Cockcroft, D.J. Latham, Ductility and the workability of metals, J. Inst. Met. Inst. Met. (1968).

[18] G.R. Johnson, W.H. Cook, Fracture characteristics of three metals subjected to various strains, strain rates, temperatures and pressures, Eng. Fract. Mech. 21 (1985) 31–48, http://dx.doi.org/10.1016/0013-7944(85)90052-9.

[19] S. Tsutsumi, T. Kitamura, R. Fincato, Ductile behaviour of carbon steel for welded structures: Experiments and numerical simulations, J. Constr. Steel Res. 172 (2020) http://dx.doi.org/10.1016/j.jcsr.2020.106185.

[20] T. Wierzbicki, Y. Bao, Y.W. Lee, Y. Bai, Calibration and evaluation of seven fracture models, Int. J. Mech. Sci. 47 (2005) 719–743, http://dx.doi.org/10.1016/j.ijmecsci.2005.03.003.

[21] M.L. Wilkins, R.D. Streit, J.E. Reaugh, Cumulative-strain-damage model of ductile fracture: simulation and prediction of engineering fracture tests, Livermore, CA, 1980. http://dx.doi.org/10.2172/6628920.

[22] K. Zhang, H. Badreddine, N. Hfaiedh, K. Saanouni, J. Liu, Enhanced CDM model accounting of stress triaxiality and Lode angle for ductile damage prediction in metal forming, Int. J. Damage Mech. 30 (2021) 260–282, http://dx.doi.org/10.1177/1056789520958045.

[23] A. Menzel, P. Steinmann, Geometrically non-linear anisotropic inelasticity based on fictitious configurations: Application to the coupling of continuum damage and multiplicative elasto-plasticity, Internat. J. Numer. Methods Engrg. 56 (2003) 2233–2266, http://dx.doi.org/10.1002/nme.662.

[24] J. Lemaitre, Coupled elasto-plasticity and damage constitutive equations, Comput. Methods Appl. Mech. Engrg. 51 (1985) 31–49, http://dx.doi.org/10.1016/0045-7825(85)90026-X.

[25] R. Fincato, S. Tsutsumi, A return mapping algorithm for elastoplastic and ductile damage constitutive equations using the subloading surface method, Internat. J. Numer. Methods Engrg. 113 (2017) 1729–1754, http://dx.doi.org/10.1002/nme.5718.

[26] T.S. Cao, J.M. Gachet, P. Montmitonnet, P.O. Bouchard, A Lode-dependent enhanced Lemaitre model for ductile fracture prediction at low stress triaxiality, Eng. Fract. Mech. 124–125 (2014) 80–96, http://dx.doi.org/10.1016/j.engfracmech.2014.03.021.
[27] H. Badreddine, Z.M. Yue, K. Saanouni, Modeling of the induced plastic anisotropy fully coupled with ductile damage under finite strains, Int. J. Solids Struct. 108 (2017) 49–62, http://dx.doi.org/10.1016/j.ijsolstr.2016.10.028.
[28] G.Z. Voyiadjis, P.I. Kattan, A plasticity-damage theory for large deformation of solids—I. Theoretical formulation, Internat. J. Engrg. Sci. 30 (1992) 1089–1108, http://dx.doi.org/10.1016/0020-7225(92)90059-P.
[29] G.Z. Voyiadjis, A. Shojaei, G. Li, P. Kattan, Continuum damage-healing mechanics with introduction to new healing variables, Int. J. Damage Mech. 21 (2012) 391–414, http://dx.doi.org/10.1177/1056789510397069.
[30] A.L. Gurson, Continuum theory of ductile rupture by void nucleation and growth: Part I—Yield criteria and flow rules for porous ductile media, J. Eng. Mater. Technol. 99 (1977) 2, http://dx.doi.org/10.1115/1.3443401.
[31] A. Needleman, V. Tvergaard, An analysis of ductile rupture in notched bars, J. Mech. Phys. Solids 32 (1984) 461–490, http://dx.doi.org/10.1016/0022-5096(84)90031-0.
[32] Z. He, H. Zhu, Y. Hu, An improved shear modified GTN model for ductile fracture of aluminium alloys under different stress states and its parameters identification, Int. J. Mech. Sci. 192 (2021) 106081, http://dx.doi.org/10.1016/j.ijmecsci.2020.106081.
[33] W. Jiang, Y. Li, J. Su, Modified GTN model for a broad range of stress states and application to ductile fracture, Eur. J. Mech. A Solids 57 (2016) 132–148, http://dx.doi.org/10.1016/j.euromechsol.2015.12.009.
[34] J.P. Pascon, H. Waisman, A thermodynamic framework to predict ductile damage in thermoviscoplastic porous metals, Mech. Mater. 153 (2021) 103701, http://dx.doi.org/10.1016/j.mechmat.2020.103701.
[35] T.S. Cao, Models for ductile damage and fracture prediction in cold bulk metal forming processes: a review, Int. J. Mater. Form. 10 (2017) 139–171, http://dx.doi.org/10.1007/s12289-015-1262-7.
[36] Y. Lou, H. Huh, Evaluation of ductile fracture criteria in a general three-dimensional stress state considering the stress triaxiality and the lode parameter, Acta Mech. Solida Sin. 26 (2013) 642–658, http://dx.doi.org/10.1016/S0894-9166(14)60008-2.
[37] J. Lin, Y. Liu, T.A. Dean, A review on damage mechanisms, models and calibration methods under various deformation conditions, Int. J. Damage Mech. 14 (2005) 299–319, http://dx.doi.org/10.1177/1056789505050357.
[38] R. Amaral, P. Teixeira, A.D. Santos, J.C. de Sá, Assessment of different ductile damage models and experimental validation, Int. J. Mater. Form. 11 (2018) 435–444, http://dx.doi.org/10.1007/s12289-017-1381-4.
[39] Z. Pater, J. Tomczak, T. Bulzak, Ł. Wójcik, P. Walczuk, Assessment of ductile fracture criteria with respect to their application in the modeling of cross wedge rolling, J. Mater Process. Technol. 278 (2020) 116501, http://dx.doi.org/10.1016/j.jmatprotec.2019.116501.
[40] K. Zhang, H. Badreddine, K. Saanouni, Ductile fracture prediction using enhanced CDM model with lode angle-dependency for titanium alloy Ti-6Al-4V at room temperature, J. Mater Process. Technol. 277 (2020) 116462, http://dx.doi.org/10.1016/j.jmatprotec.2019.116462.
[41] A. Neimitz, J. Galkiewicz, S. Lipiec, I. Dzioba, Estimation of the onset of crack growth in ductile materials, Materials (Basel) 11 (2018) 2026, http://dx.doi.org/10.3390/ma11102026.
[42] J. Zhou, X. Gao, J.C. Sobotka, B.A. Webler, B.V. Cockeram, On the extension of the Gurson-type porous plasticity models for prediction of ductile fracture under shear-dominated conditions, Int. J. Solids Struct. 51 (2014) 3273–3291, http://dx.doi.org/10.1016/j.ijsolstr.2014.05.028.
[43] L. Xue, Constitutive modeling of void shearing effect in ductile fracture of porous materials, Eng. Fract. Mech. 75 (2008) 3343–3366, http://dx.doi.org/10.1016/j.engfracmech.2007.07.022.
[44] L. Cortese, F. Nalli, M. Rossi, A nonlinear model for ductile damage accumulation under multiaxial non-proportional loading conditions, Int. J. Plast. 85 (2016) 77–92, http://dx.doi.org/10.1016/j.ijplas.2016.07.003.
[45] L. Cheng, V. Monchiet, L. Morin, G. de Saxcé, D. Kondo, An analytical Lode angle dependent damage model for ductile porous materials, Eng. Fract. Mech. 149 (2015) 119–133, http://dx.doi.org/10.1016/j.engfracmech.2015.09.038.
[46] C.C. Roth, D. Mohr, Ductile fracture experiments with locally proportional loading histories, Int. J. Plast. 79 (2016) 328–354, http://dx.doi.org/10.1016/j.ijplas.2015.08.004.
[47] R. Balieu, N. Kringos, A new thermodynamical framework for finite strain multiplicative elastoplasticity coupled to anisotropic damage, Int. J. Plast. 70 (2015) 126–150, http://dx.doi.org/10.1016/j.ijplas.2015.03.006.
[48] H. Badreddine, K. Saanouni, On the full coupling of plastic anisotropy and anisotropic ductile damage under finite strains, Int. J. Damage Mech. 26 (2017) 1080–1123, http://dx.doi.org/10.1177/1056789516635729.
[49] P.J. Noell, J.D. Carroll, B.L. Boyce, The mechanisms of ductile rupture, Acta Mater. 161 (2018) 83–98, http://dx.doi.org/10.1016/j.actamat.2018.09.006.
[50] L. Ying, D. Wang, W. Liu, Y. Wu, P. Hu, On the numerical implementation of a shear modified GTN damage model and its application to small punch test, Int. J. Mater. Form. 11 (2018) 527–539, http://dx.doi.org/10.1007/s12289-017-1362-7.
[51] A.S. Khan, A. Pandey, T. Stoughton, Evolution of subsequent yield surfaces and elastic constants with finite plastic deformation. Part II: A very high work hardening aluminum alloy (annealed 1100 Al), Int. J. Plast. 26 (2010) 1421–1431, http://dx.doi.org/10.1016/j.ijplas.2009.07.008.
[52] H. Badreddine, K. Saanouni, T.D. Nguyen, Damage anisotropy and its effect on the plastic anisotropy evolution under finite strains, Int. J. Solids Struct. 63 (2015) 11–31, http://dx.doi.org/10.1016/j.ijsolstr.2015.02.009.
[53] W. Rajhi, K. Saanouni, H. Sidhom, Anisotropic ductile damage fully coupled with anisotropic plastic flow: Modeling, experimental validation, and application to metal forming simulation, Int. J. Damage Mech. 23 (2014) 1211–1256, http://dx.doi.org/10.1177/1056789514524076.
[54] H. Zhang, H. Zhang, F. Li, J. Cao, A novel damage model to predict ductile fracture behavior for anisotropic sheet metal, Metals (Basel) 9 (2019) 595, http://dx.doi.org/10.3390/met9050595.

[55] R. Hill, A theory of the yielding and plastic flow of anisotropic metals, Proc. R. Soc. A 193 (1948) 281–297, http://dx.doi.org/10.1098/rspa.1948.0045.
[56] S.A. Habib, J.T. Lloyd, C.S. Meredith, A.S. Khan, S.E. Schoenfeld, Fracture of an anisotropic rare-earth-containing magnesium alloy (ZEK100) at different stress states and strain rates: Experiments and modeling, Int. J. Plast. 122 (2019) 285–318, http://dx.doi.org/10.1016/j.ijplas.2019.07.011.
[57] R. Fincato, S. Tsutsumi, An overstress elasto-viscoplasticity model for high/low cyclic strain rates loading conditions: part I - formulation and computational aspects, Int. J. Solids Struct. (2020) http://dx.doi.org/10.1016/j.ijsolstr.2020.10.013.
[58] R. Fincato, S. Tsutsumi, An overstress elasto-viscoplasticity model for high/low cyclic strain rates loading conditions: Part II – Numerical analyses, Int. J. Solids Struct. 208–209 (2021) 247–261, http://dx.doi.org/10.1016/j.ijsolstr.2020.11.010.
[59] J.L. Chaboche, Time-independent constitutive theories for cyclic plasticity, Int. J. Plast. 2 (1986) 149–188, http://dx.doi.org/10.1016/0749-6419(86)90010-0.
[60] J. Lemaitre, A continuous damage mechanics model for ductile fracture, J. Eng. Mater. Technol. 107 (1985) 83, http://dx.doi.org/10.1115/1.3225775.
[61] Y. Jiao, J. Fish, On the equivalence between the multiplicative hyper-elasto-plasticity and the additive hypo-elasto-plasticity based on the modified kinetic logarithmic stress rate, Comput. Methods Appl. Mech. Engrg. 340 (2018) 824–863, http://dx.doi.org/10.1016/j.cma.2018.06.017.
[62] Y. Jiao, J. Fish, Is an additive decomposition of a rate of deformation and objective stress rates passé? Comput. Methods Appl. Mech. Engrg. 327 (2017) 196–225, http://dx.doi.org/10.1016/j.cma.2017.07.021.
[63] R. Fincato, S. Tsutsumi, Numerical modeling of the evolution of ductile damage under proportional and non-proportional loading, Int. J. Solids Struct. 160 (2019) 247–264, http://dx.doi.org/10.1016/j.ijsolstr.2018.10.028.
[64] R. Fincato, S. Tsutsumi, Closest-point projection method for the extended subloading surface model, Acta Mech. 228 (12) (2017) 4213–4233, http://dx.doi.org/10.1007/s00707-017-1926-0.
[65] R. Fincato, S. Tsutsumi, Numerical study of a welded plate instability using the subloading surface model, Mar. Struct. 55 (2017) 104–120, http://dx.doi.org/10.1016/j.marstruc.2017.05.001.
[66] T. Brepols, I.N. Vladimirov, S. Reese, Numerical comparison of isotropic hypo- and hyperelastic-based plasticity models with application to industrial forming processes, Int. J. Plast. 63 (2014) 18–48, http://dx.doi.org/10.1016/j.ijplas.2014.06.003.
[67] H. Badreddine, K. Saanouni, A. Dogui, On non-associative anisotropic finite plasticity fully coupled with isotropic ductile damage for metal forming, Int. J. Plast. 26 (2010) 1541–1575, http://dx.doi.org/10.1016/j.ijplas.2010.01.008.
[68] K. Hashiguchi, M. Ueno, Elastoplastic constitutive laws of granular materials, Constitutive Equations of Soils, in: S. Murayama, A.N. Schoefield (Eds.), Proc. 9th Int. Conf. Soil Mech. Found. Eng., Spec. Ses. 9, Tokyo, 1977, pp. 73–82.
[69] K. Hashiguchi, Subloading surface model in unconventional plasticity, Int. J. Solids Struct. 25 (1989) 917–945, http://dx.doi.org/10.1016/0020-7683(89)90038-3.
[70] K. Hashiguchi, Foundations of Elastoplasticity: Subloading Surface Model, 2017, http://dx.doi.org/10.1007/978-3-319-48821-9.
[71] J.C. Simo, T.J.R. Hughes, Computational Inelasticity, Springer-Verlag, New York, 1998, http://dx.doi.org/10.1007/b98904.
[72] J.K. Dienes, On the analysis of rotation and stress rate in deforming bodies, Acta Mech. 32 (1979) 217–232, http://dx.doi.org/10.1007/BF01379008.
[73] M. Brünig, V. Hagenbrock, S. Gerke, Macroscopic damage laws based on analysis of microscopic unit cells, ZAMM - J. Appl. Math. Mech. / Z. Angew. Math. Mech. 98 (2018) 181–194, http://dx.doi.org/10.1002/zamm.201700188.
[74] M. Brünig, A thermodynamically consistent continuum damage model taking into account the ideas of CL Chow, Int. J. Damage Mech. 25 (2016) 1130–1141, http://dx.doi.org/10.1177/1056789516639119.
[75] C.L. Chow, Y. Wei, Constitutive modeling of material damage for fatigue failure prediction, Int. J. Damage Mech. 8 (1999) 355–375, http://dx.doi.org/10.1177/105678959900800405.
[76] J.L. Chaboche, Continuum damage mechanics: Part I - General concepts, J. Appl. Mech. Trans. ASME 55 (1988) 59–64, http://www.scopus.com/inward/record.url?eid=2-s2.0-0023978287&partnerID=tZOtx3y1.
[77] J. Besson, S. Forest, G. Cailletaud, M. Blétry, J.L. Chaboche, Non-linear mechanics of materials, Solid Mech. Appl. (2010) http://dx.doi.org/10.1007/978-90-481-3356-7_1.
[78] R. De Borst, P.H. Feenstra, Studies in anisotropic plasticity with reference to the Hill criterion, Internat. J. Numer. Methods Engrg. 29 (1990) 315–336, http://dx.doi.org/10.1002/nme.1620290208.
[79] J. Lemaitre, R. Desmorat, Engineering Damage Mechanics: Ductile, Creep, Fatigue and Brittle Failures, Springer Berlin Heidelberg, 2005, http://dx.doi.org/10.1007/b138882.
[80] M. Brünig, S. Gerke, V. Hagenbrock, Stress-state-dependence of damage strain rate tensors caused by growth and coalescence of micro-defects, Int. J. Plast. 63 (2014) 49–63, http://dx.doi.org/10.1016/j.ijplas.2014.04.007.
[81] Y. Bao, T. Wierzbicki, On fracture locus in the equivalent strain and stress triaxiality space, Int. J. Mech. Sci. 46 (2004) 81–98, http://dx.doi.org/10.1016/j.ijmecsci.2004.02.006.
[82] F.A. McClintock, A criterion for ductile fracture by the growth of holes, J. Appl. Mech. 35 (1968) 363, http://dx.doi.org/10.1115/1.3601204.
[83] M.L. Wilkins, Calculation of Elastic-Plastic Flow, Vol. 3, B., Academic Press, New York, 1964.
[84] L. Malcher, E.N. Mamiya, An improved damage evolution law based on continuum damage mechanics and its dependence on both stress triaxiality and the third invariant, Int. J. Plast. 56 (2014) 232–261, http://dx.doi.org/10.1016/j.ijplas.2014.01.002.
[85] G. Mirone, R. Barbagallo, D. Corallo, A new yield criteria including the effect of lode angle and stress triaxiality, Procedia Struct. Integr. 2 (2016) 3684–3696, http://dx.doi.org/10.1016/j.prostr.2016.06.458.
[86] L.S. Costin, Damage mechanics in the post-failure regime, Mech. Mater. 4 (1985) 149–160, http://dx.doi.org/10.1016/0167-6636(85)90013-4.

[87] Y.N. Rabotnov, Creep rupture, in: Appl. Mech., Springer Berlin Heidelberg, Berlin, Heidelberg, 1969, pp. 342–349, http://dx.doi.org/10.1007/978-3-642-85640-2_26.
[88] M. Brünig, An anisotropic ductile damage model based on irreversible thermodynamics, Int. J. Plast. 19 (2003) 1679–1713, http://dx.doi.org/10.1016/S0749-6419(02)00114-6.
[89] R. Desmorat, S. Cantournet, Modeling microdefects closure effect with isotropic/anisotropic damage, Int. J. Damage Mech. 17 (2008) 65–96, http://dx.doi.org/10.1177/1056789507069541.
[90] Y. Murakami, Material defects as the basis of fatigue design, Int. J. Fatigue (2012) http://dx.doi.org/10.1016/j.ijfatigue.2011.12.001.
[91] J.L. Chaboche, Continuum damage mechanics, J. Appl. Mech. 55 (1988) 65–72, http://dx.doi.org/10.1115/1.3173662, T4 - Part II—Damage Growth, Crack Initiation, and Crack Growth M4 - Citavi.
[92] M. Ortiz, A constitutive theory for the inelastic behavior of concrete, Mech. Mater. 4 (1985) 67–93, http://dx.doi.org/10.1016/0167-6636(85)90007-9.
[93] S. Tsutsumi, M. Toyosada, K. Hashiguchi, Extended subloading surface model incorporating elastic boundary concept, J. Appl. Mech. 9 (2006) 455–462, http://dx.doi.org/10.2208/journalam.9.455.
[94] A.S. Khan, S. Huang, Continuum Theory of Plasticity, Wiley-Interscience, 1995.
[95] G. Jaumann, Geschlossenes system physikalischer und chemischer differentialgesetze, Math.-Nat. Sitz.ber. Wiener Akad. Wiss. (1911).
[96] A.E. Green, P.M. Naghdi, A general theory of an elastic–plastic continuum, Arch. Ration. Mech. Anal. (1965) http://dx.doi.org/10.1007/BF00251666.
[97] S. Tsutsumi, R. Fincato, H. Momii, Effect of tangential plasticity on structural response under non-proportional cyclic loading, Acta Mech. (2019) http://dx.doi.org/10.1007/s00707-019-02398-8.
[98] D.K. Kim, J.W. Hu, Comparison of various object stress rates under simple shear, Adv. Mater. Res. 650 (2013) 407–413, http://dx.doi.org/10.4028/www.scientific.net/AMR.650.407.
[99] Z.P. Bažant, J. Vorel, Energy-conservation error due to use of Green–Naghdi objective stress rate in commercial finite-element codes and its compensation, J. Appl. Mech. 81 (2014) http://dx.doi.org/10.1115/1.4024411.
[100] A. Beghini, Z.P. Bažant, R. Chambon, D. Kolymbas, I. Herle, Shear and objective stress rates in hypoplasticity by D. Kolymbas and I. HerleAuthor's reply to discussion by A. Beghini and Z. P. Bazant, R. Chambon and A. Niemunis of 'Shear and objective stress rates in hypoplasticity', Int. J. Numer. Anal. Methods Geomech. 28 (2004) 365–372, http://dx.doi.org/10.1002/nag.337.
[101] L. Szabó, M. Balla, Comparison of some stress rates, Int. J. Solids Struct. 25 (1989) 279–297, http://dx.doi.org/10.1016/0020-7683(89)90049-8.
[102] D. Perić, On consistent stress rates in solid mechanics: Computational implications, Internat. J. Numer. Methods Engrg. 33 (1992) 799–817, http://dx.doi.org/10.1002/nme.1620330409.
[103] Y.F. Dafalias, Corotational rates for kinematic hardening at large plastic deformations, J. Appl. Mech. 50 (1983) 561, http://dx.doi.org/10.1115/1.3167091.
[104] J.C. Simo, K.S. Pister, Remarks on rate constitutive equations for finite deformation problems: computational implications, Comput. Methods Appl. Mech. Engrg. 46 (1984) 201–215, http://dx.doi.org/10.1016/0045-7825(84)90062-8.
[105] M. Kojić, K.-J. Bathe, Studies of finite element procedures—Stress solution of a closed elastic strain path with stretching and shearing using the updated Lagrangian Jaumann formulation, Comput. Struct. 26 (1987) 175–179, http://dx.doi.org/10.1016/0045-7949(87)90247-1.
[106] H. Xiao, O.T. Bruhns, A. Meyers, Logarithmic strain, logarithmic spin and logarithmic rate, Acta Mech. 124 (1997) 89–105, http://dx.doi.org/10.1007/BF01213020.
[107] H. Xiao, O.T. Bruhns, A. Meyers, On objective corotational rates and their defining spin tensors, Int. J. Solids Struct. 35 (1998) 4001–4014, http://dx.doi.org/10.1016/S0020-7683(97)00267-9.
[108] Y. Zhu, G. Kang, Q. Kan, O.T. Bruhns, Logarithmic stress rate based constitutive model for cyclic loading in finite plasticity, Int. J. Plast. 54 (2014) 34–55, http://dx.doi.org/10.1016/j.ijplas.2013.08.004.
[109] R.J. Asaro, Micromechanics of crystals and polycrystals, Adv. Appl. Mech. (1983) http://dx.doi.org/10.1016/S0065-2156(08)70242-4.
[110] Y. Zhu, G. Kang, C. Yu, A finite cyclic elasto-plastic constitutive model to improve the description of cyclic stress–strain hysteresis loops, Int. J. Plast. 95 (2017) http://dx.doi.org/10.1016/j.ijplas.2017.04.009.
[111] M. Trajković-Milenković, O.T. Bruhns, A. Zorić, On instability of constitutive models for isotropic elastic-perfectly plastic material behaviour at finite deformations, Proc. Inst. Mech. Eng. C (2020) 095440622092068, http://dx.doi.org/10.1177/0954406220920687.
[112] D. Soldatos, S.P. Triantafyllou, Logarithmic spin, logarithmic rate and material frame-indifferent generalized plasticity, Int. J. Appl. Mech. 08 (2016) 1650060, http://dx.doi.org/10.1142/S1758825116500605.
[113] S.-Y. Wang, L. Zhan, H.-F. Xi, O.T. Bruhns, H. Xiao, Hencky strain and logarithmic rate for unified approach to constitutive modeling of continua, in: Adv. Struct. Mater., Vol 100, Springer, Cham, 2019, pp. 443–484, http://dx.doi.org/10.1007/978-3-030-30355-6_19.
[114] H.M. Zbib, E.C. Aifantis, On the concept of relative and plastic spins and its implications to large deformation theories. Part I: Hypoelasticity and vertex-type plasticity, Acta Mech. 75 (1988) 15–33, http://dx.doi.org/10.1007/BF01174625.
[115] Y.F. Dafalias, The plastic spin, J. Appl. Mech. 52 (1985) 865–871, http://dx.doi.org/10.1115/1.3169160.
[116] L. Duchene, T. Lelotte, P. Flores, S. Bouvier, A. Habraken, Rotation of axes for anisotropic metal in FEM simulations, Int. J. Plast. 24 (2008) 397–427, http://dx.doi.org/10.1016/j.ijplas.2007.03.015.
[117] E.L. Bonnaud, P. Gudmundson, Lead-free solder cyclic plasticity characterization for drop test simulations, in: 7th. Int. Conf. Therm. Mech. Multiphysics Simul. Exp. Micro-Electronics Micro-Systems, IEEE, 2006, pp. 1–4, http://dx.doi.org/10.1109/ESIME.2006.1644023.
[118] A.R. Khoei, M. Eghbalian, Numerical simulation of cyclic behavior of ductile metals with a coupled damage–viscoplasticity model, Comput. Mater. Sci. 55 (2012) 376–389, http://dx.doi.org/10.1016/j.commatsci.2011.12.008.

[119] L.M. Kachanov, Time of the rupture process under creep conditions, Izv. Akad. Nauk. SSR Otd. Tech. Nauk. 8 (1958) 26–31, doi:citeulike-article-id:5466815.
[120] Y. Hammi, M.F. Horstemeyer, A physically motivated anisotropic tensorial representation of damage with separate functions for void nucleation, growth, and coalescence, Int. J. Plast. 23 (2007) 1641–1678, http://dx.doi.org/10.1016/j.ijplas.2007.03.010.
[121] F.X.C. Andrade, J.M.A. César de Sá, F.M. Andrade Pires, A ductile damage nonlocal model of integral-type at finite strains: Formulation and numerical issues, Int. J. Damage Mech. 20 (2011) 515–557, http://dx.doi.org/10.1177/1056789510386850.
[122] F. Marotti de Sciarra, Hardening plasticity with nonlocal strain damage, Int. J. Plast. 34 (2012) 114–138, http://dx.doi.org/10.1016/j.ijplas.2012.01.009.
[123] F. Marotti de Sciarra, A nonlocal model with strain-based damage, Int. J. Solids Struct. 46 (2009) 4107–4122, http://dx.doi.org/10.1016/j.ijsolstr.2009.08.009.
[124] L. Sprave, A. Menzel, A large strain gradient-enhanced ductile damage model: finite element formulation, experiment and parameter identification, Acta Mech. 231 (2020) 5159–5192, http://dx.doi.org/10.1007/s00707-020-02786-5.
[125] K. Saanouni, M. Hamed, Micromorphic approach for finite gradient-elastoplasticity fully coupled with ductile damage: Formulation and computational aspects, Int. J. Solids Struct. 50 (2013) 2289–2309, http://dx.doi.org/10.1016/j.ijsolstr.2013.03.027.
[126] T. Brepols, S. Wulfinghoff, S. Reese, Gradient-extended two-surface damage-plasticity: Micromorphic formulation and numerical aspects, Int. J. Plast. 97 (2017) 64–106, http://dx.doi.org/10.1016/j.ijplas.2017.05.010.
[127] R. Alessi, J.-J. Marigo, S. Vidoli, Gradient damage models coupled with plasticity: Variational formulation and main properties, Mech. Mater. 80 (2015) 351–367, http://dx.doi.org/10.1016/j.mechmat.2013.12.005.
[128] L. Sprave, A. Menzel, Gradient-enhanced ductile damage — a finite deformation framework with application to DP800, PAMM 18 (2018) http://dx.doi.org/10.1002/pamm.201800232.
[129] J. Lee, S.-J. Kim, H. Park, H.J. Bong, D. Kim, Metal plasticity and ductile fracture modeling for cast aluminum alloy parts, J. Mater Process. Technol. 255 (2018) 584–595, http://dx.doi.org/10.1016/j.jmatprotec.2017.12.040.
[130] B.C. Cerik, J. Choung, Ductile fracture behavior of mild and high-tensile strength shipbuilding steels, Appl. Sci. 10 (2020) 7034, http://dx.doi.org/10.3390/app10207034.
[131] F.M. Andrade Pires, E.A. de Souza Neto, D.R.J. Owen, On the finite element prediction of damage growth and fracture initiation in finitely deforming ductile materials, Comput. Methods Appl. Mech. Engrg. 193 (2004) 5223–5256, http://dx.doi.org/10.1016/j.cma.2004.01.038.
[132] M. Kumar, P.M. Dixit, A nonlinear ductile damage growth law, Int. J. Damage Mech. 24 (2015) 1070–1085, http://dx.doi.org/10.1177/1056789514561807.
[133] Z. Yue, K. Cao, H. Badreddine, K. Saanouni, J. Gao, Failure prediction on steel sheet under different loading paths based on fully coupled ductile damage model, Int. J. Mech. Sci. 153–154 (2019) 1–9, http://dx.doi.org/10.1016/j.ijmecsci.2019.01.029.
[134] A. Benaarbia, J.P. Rouse, W. Sun, A thermodynamically-based viscoelastic-viscoplastic model for the high temperature cyclic behaviour of 9%–12% Cr steels, Int. J. Plast. 107 (2018) 100–121, http://dx.doi.org/10.1016/j.ijplas.2018.03.015.
[135] P. Oppermann, R. Denzer, A. Menzel, Finite-strain thermo-viscoplasticity for case-hardening steels over a wide temperature range, PAMM 19 (2019) http://dx.doi.org/10.1002/pamm.201900237.
[136] S. Roy Chowdhury, G. Kar, D. Roy, J.N. Reddy, Metal viscoplasticity with two-temperature thermodynamics and two dislocation densities, Contin. Mech. Thermodyn. 30 (2018) 397–420, http://dx.doi.org/10.1007/s00161-017-0606-6.
[137] S. Roy Chowdhury, G. Kar, D. Roy, J.N. Reddy, Two-temperature thermodynamics for metal viscoplasticity: Continuum modeling and numerical experiments, J. Appl. Mech. 84 (2017) http://dx.doi.org/10.1115/1.4034726.
[138] T.J.R. Hughes, J. Winget, Finite rotation effects in numerical integration of rate constitutive equations arising in large-deformation analysis, Internat. J. Numer. Methods Engrg. 15 (1980) 1862–1867, http://dx.doi.org/10.1002/nme.1620151210.
[139] M. Palizi, S. Federico, S. Adeeb, Consistent numerical implementation of hypoelastic constitutive models, Z. Angew. Math. Phys. 71 (2020) 156, http://dx.doi.org/10.1007/s00033-020-01335-3.
[140] R. Fincato, S. Tsutsumi, A numerical study of the return mapping application for the subloading surface model, Eng. Comput. 35 (2018) 1314–1343, http://dx.doi.org/10.1108/EC-12-2016-0446.